

Novel Clustering Schemes for Full and Compact Polarimetric SAR Data: An Application for Rice Phenology Characterization

Subhadip Dey^{a,*}, Avik Bhattacharya^a, Debanshu Ratha^a,
Dipankar Mandal^a, Heather McNairn^b, Juan M. Lopez-Sanchez^c, Y. S. Rao^a

^a*Microwave Remote Sensing Lab, CSRE, Indian Institute of Technology Bombay,
Mumbai, India*

^b*Ottawa Research and Development Centre, Agriculture and Agri-Food Canada, Canada*

^c*University of Alicante, Alicante, Spain*

Abstract

Information on rice phenological stages from Synthetic Aperture Radar (SAR) images is of prime interest for in-season monitoring. Often, prior in-situ measurements of phenology are not available. In such situations, unsupervised clustering of SAR images might help in discriminating phenological stages of a crop throughout its growing period. Among the existing unsupervised clustering techniques using full-polarimetric (FP) SAR images, the eigenvalue-eigenvector based roll-invariant scattering-type parameter, and the scattering entropy parameter are widely used in the literature. In this study, we utilize a unique target scattering-type parameter, which jointly uses the Barakat degree of polarization and the elements of the polarimetric coherency matrix. Likewise, we also utilize an equivalent parameter proposed for compact-polarimetric (CP) SAR data. These scattering-type parameters are analogous to the Cloude-Pottier's parameter for FP SAR data and the

*Corresponding author: Subhadip Dey (sdey2307@gmail.com)

ellipticity parameter for CP SAR data. Besides this, we also introduce new clustering schemes for both FP and CP SAR data for segmenting diverse scattering mechanisms across the phenological stages of rice. In this study, we use the RADARSAT-2 FP and simulated CP SAR data acquired over the Indian test site of Vijayawada under the Joint Experiment for Crop Assessment and Monitoring (JECAM) initiative. The temporal analysis of the scattering-type parameters and the new clustering schemes help us to investigate detailed scattering characteristics from rice across its phenological stages.

Keywords: Unsupervised clustering, Entropy, RADARSAT-2, Crop monitoring, PolSAR, Roll-invariant parameter

1. Introduction

Variations in crop phenological stages can be characterized by Synthetic Aperture Radar (SAR) data due to its high sensitivity to the dielectric and geometrical structure of the canopy. However, depending on the frequency of the transmitted electromagnetic (EM) wave, the interaction with crop canopy layers and the underlying soil varies significantly (Davidson et al., 2000). Previous studies reported that phenological changes could be adequately captured with high-frequency SAR sensors utilizing backscattered information from vegetation canopy (Wiseman et al., 2014; De Bernardis et al., 2015; McNairn and Shang, 2016; McNairn et al., 2018). In general, the SAR backscatter signal might be affected by the underlying surface during early vegetative growth stages when the canopy was sparse and open (Paloscia, 2002).

14 One of the primary parameters associated with the changes in the SAR
 15 backscatter coefficient is the crop canopy distribution (e.g., tillers, leaves, and
 16 panicles) at each phenological stage. Moreover, this distribution in the crop
 17 fields also leads to randomness in scattering (Yuzugullu et al., 2015). In such
 18 situations, polarimetric entropy (H) is an important parameter to quantify
 19 this randomness. In Cloude and Pottier (1997), an unsupervised classification
 20 scheme ($H/\bar{\alpha}$) was proposed using H and the average scattering-type param-
 21 eter ($\bar{\alpha}$). The $H/\bar{\alpha}$ plane is sub-divided into nine zones to suitably cluster
 22 various scattering mechanisms. The properties of different scattering mech-
 23 anisms determine the boundaries between the zones. Hence certain assump-
 24 tions are utilized in the proper setting of these boundaries. Subsequently, the
 25 2D clustering plane is extended to 3D $H/A/\bar{\alpha}$ space by introducing the scat-
 26 tering anisotropy parameter A . This parameter, which is complementary to
 27 H , is useful to discriminate targets when $H > 0.7$. However, for lower values
 28 of H , this parameter is noisy and could introduce inaccuracies in determining
 29 the clusters.

30 Lopez-Sanchez et al. (2011) reported the importance of the $H/\bar{\alpha}$ plane to
 31 discriminate phenological stages of rice along with the temporal correlation
 32 of HH and VV and their ratio. The clustering results show that at the
 33 beginning of the cultivation period of rice, the data cluster was denser in
 34 the region with medium entropy and low alpha, which was primarily due to
 35 the presence of sparse vegetation in the fields. However, at the advanced
 36 phenological stages, the cluster density shifted towards the region of high
 37 entropy and high alpha in the $H/\bar{\alpha}$ plane.

38 In another study, Lopez-Sanchez et al. (2012) utilized the dominant scattering-

39 type information (α_1) instead of $\bar{\alpha}$. In this study, the temporal behaviour of
40 α_1 and the scattering entropy was shown with the phenological stages of rice.
41 At the initial stage, α_1 and entropy were both within low to medium values,
42 and they jointly increased during the plant emergence stage. During the
43 advanced vegetative stage, both parameters show the dominance of multiple
44 scattering from the fields. In contrast, at the harvest stage, $\alpha_1 < 30^\circ$ and
45 the scattering entropy remained high due to the field roughness condition.

46 Praks et al. (2009) proposed alternative scattering-type and randomness
47 parameters equivalent to $\bar{\alpha}$ and H for clustering PolSAR data. These pa-
48 rameters can be directly obtained from the elements of the coherency matrix
49 without utilizing the eigenvalues and the eigenvectors. It was shown that in-
50 stead of $\bar{\alpha}$ and H , the surface scattering fraction and the scattering diversity
51 that are equivalent polarimetric descriptors can be utilized for classification,
52 visualization, or interpretation. Later, Yin et al. (2015) proposed a new
53 parameter, α_B , defined by the co-polarization ratio and their coherence to
54 capture various scattering mechanisms. This new parameter was able to dis-
55 tinguish scattering from oriented and randomly distributed targets. In their
56 study a new $\Delta\alpha_B/\alpha_B$ plane was proposed which showed better separation ca-
57 pability than the $H/\bar{\alpha}$ clustering plane. It was also stated that the stability
58 of the proposed method was better with multi-temporal SAR data.

59 In another work, Ratha et al. (2019) proposed a roll-invariant scattering-
60 type parameter (α_{GD}), the helicity parameter (τ_{GD}), and the purity parame-
61 ter (P_{GD}) using a geodesic distance between two Kennaugh matrices. A new
62 P_{GD}/α_{GD} unsupervised classification scheme is proposed which is analogous
63 to $H/\bar{\alpha}$. However, the P_{GD}/α_{GD} clustering plane showed better performance

64 than earlier proposed schemes.

65 The study using compact-polarimetric (CP) SAR data holds promise
66 due to the upcoming constellation of satellites such as the Canadian RAD-
67 ARSAT Constellation Mission (RCM), SAOCOM (TOPSAR with experi-
68 mental CP-mode), and the NISAR (the NASA-ISRO SAR) L- and S-band
69 mission. Similar to the full-polarimetric (FP) case, scattering-type clustering
70 assessment using compact polarimetric (CP) SAR data and its decomposition
71 parameters (Raney, 2007; Cloude et al., 2011; Raney et al., 2012) are lately
72 gaining interest (Ainsworth et al., 2009; Charbonneau et al., 2010; Ballester-
73 Berman and Lopez-Sanchez, 2011; Sabry and Vachon, 2013). Brisco et al.
74 (2013) assessed hybrid-compact, circular, and linear polarimetric SAR data
75 for rice and wetlands mapping. Also, different dual-channel combinations and
76 $m - \delta$ decomposition parameters for CP data were assessed in their study,
77 where the classification accuracy for CP data was comparatively better than
78 linear dual-polarimetric SAR data.

79 Lopez-Sanchez et al. (2014) used the radar backscatter coefficients and
80 the $H/\bar{\alpha}$ plane to investigate the dynamics of rice phenological changes for
81 full, dual, and compact polarimetric SAR data. In this study, the dominant
82 scattering-type parameter (α_s) for CP data is used instead of $\bar{\alpha}$. For CP data,
83 the entropy, in particular, is equivalent to the Barakat degree of polarization.
84 It was noticed that the pattern of α_s was similar for full, dual, and compact
85 polarimetric SAR data for rice crops. Alongside this, it was also observed
86 that α_s precisely provides similar information like the FP mode, throughout
87 the phenological cycle of rice.

88 Subsequently, Yang et al. (2014) showed improved classification accuracy

89 in discriminating transplanted and direct-sown rice fields. In this study, the
90 use of the $m - \chi$ decomposition parameters along with α_s , the degree of
91 polarization (m), relative phase (δ) and conformity coefficient (μ) improved
92 the classification accuracy from 88 % to 95 %. Besides, the classification
93 accuracy confirmed the advantage of CP data over other dual-polarized SAR
94 data. Several other studies (Xie et al., 2015; Uppala et al., 2015; Guo et al.,
95 2018; Kumar et al., 2020) also indicated the potential of CP SAR data for
96 rice mapping and monitoring.

97 Recently, Yin et al. (2019) proposed a new parameter, α_{BCP} , for improve-
98 ment in the clustering results for land-cover features. In particular, α_{BCP} is
99 rotation-invariant and $\Delta\alpha_{BCP}/\alpha_{BCP}$ resembles the existing $\Delta\alpha_B/\alpha_B$ clus-
100 tering for FP SAR data. However, the differences between α_{BCP} and α_B
101 depend on the polarization of the received wave. Moreover, the derivation
102 of specific scattering models is needless for separate CP modes. It was also
103 observed that circular CP data provides almost similar results as FP data
104 for various scattering targets.

105 The literature, as mentioned above, provides a vital foundation for the
106 utilization of H and the scattering-type parameters (i.e., $\bar{\alpha}$ and α_s) for rice
107 crop monitoring and mapping using FP and CP SAR data. Nevertheless,
108 these techniques are formulated either by fitting scattering models or by di-
109 agonalizing the coherency (or covariance) matrix of the received wave. Hence,
110 these techniques might miss the received antenna basis invariant information
111 while characterizing various targets. The importance of the received antenna
112 basis invariant information in terms of the degree of polarization helps to
113 effectively exploit complete information from SAR data (Touzi et al., 2015,

114 2018).

115 In this study, our main objective is to characterize changes in scatter-
116 ing mechanisms utilizing the temporal series of full- and compact polari-
117 metric SAR data across the growth stages of rice. The received antenna
118 basis invariant information, i.e., in particular, the Barakat degree of polar-
119 ization (Barakat, 1977, 1983) is useful to capture changes in scattering ran-
120 domness due to crop foliage development. At the same time, the elements
121 of the coherency (or, covariance) matrices provide information about crop
122 canopy geometry as well as the soil and vegetation water content. In this re-
123 gard, a new scattering-type parameter is derived by jointly using the received
124 antenna basis invariant information and elements of coherency (or, covari-
125 ance) matrix for both FP and CP SAR data. Alongside this, we present a
126 comparative study of the performance of novel clustering schemes for FP and
127 CP data for rice phenology mapping. It is noteworthy that the formulation
128 of this new scattering-type parameter is equivalent for both FP and CP SAR
129 data.

130 Here, we have proposed new clustering schemes using θ_{FP} and θ_{CP} along
131 with H for both FP and CP SAR data, respectively. Unlike the H/α plane,
132 the proposed segmentation scheme utilizes a polar representation, which of-
133 fers a natural choice. Suitable entropy apportionment (radially) together
134 with angular extent of $\theta_X \in [-90^\circ, 90^\circ]$ (where the subscript X is either FP
135 or CP) provides a reliable target discrimination strategy. The segmentation
136 scheme produces 12 feasible clustering zones that better characterize natural
137 and human-made targets. The usefulness and performance of the scattering-
138 type parameters θ_{FP} and θ_{CP} , along with the new clustering schemes, are

assessed by utilizing them with the time-series C-band RADARSAT-2 data for monitoring rice.

2. Study area and field measurement

The study area is located near Vijayawada in the state of Andhra Pradesh, India ($16^{\circ}24'6.2''N, 8^{\circ}41'2.4''E$) as shown in figure 1 (Mandal et al., 2019). The climatic zone of this area varies from sub-humid to humid, with mostly clayey soil texture. Areal coverage of this test site is $\approx 25 \times 25 \text{ km}^2$. Rice is one of the primary and major crops cultivated in this area. The sowing period of rice varies from mid of June to mid of July depending on the variety and cultivation practices. Majorly, the cultivation starts after the pre-monsoon rain and is harvested during mid-December. The average size of each field was $\approx 60 \times 60 \text{ m}^2$, and in each field, two sampling locations were chosen for in-situ measurements. Information about the crop growth stages, management practices, and biophysical parameters was noted during the field campaign from June to December 2018.

Table 1: Statistics (mean \pm standard deviation) of bio-physical and soil parameters at different phenology stages of rice. Here, PH: plant height, PAI: plant area index, SM: soil moisture and Nan: Not a number

Date	PH (cm)	PAI ($\text{m}^2 \text{ m}^{-2}$)	SM(%)	Growth stage
05/07/2018	Nan	Nan	35.92 ± 6.6	Bare field
29/07/2018	26.30 ± 5.21	0.40 ± 0.20	Saturated	Early tillering
22/08/2018	46.26 ± 9.12	1.76 ± 0.26	Saturated	Advanced tillering
09/10/2018	92.16 ± 5.76	4.03 ± 0.20	Saturated	Flowering
02/11/2018	95.93 ± 7.76	4.06 ± 0.16	47.60 ± 0.42	Early dough
26/11/2018	98.32 ± 6.82	3.86 ± 0.22	45.16 ± 6.04	Maturity

154 A total number of 14 in-situ field measurements were considered in this
 155 study. We measured soil moisture at each field in two sampling locations,
 156 arranged in two parallel transects along the row direction. The separation
 157 between each transect was ≈ 40 m. We measured the pointwise soil moisture
 158 using theta-probe. Nevertheless, the soil underlying the rice crops was satu-
 159 rated during the majority of the growth stages due to irrigation and rainfall
 160 events. We measured vegetation samples at two points of each field due to
 161 the spatial heterogeneity within the field, which is due to the irregular growth
 162 pattern of rice. Vegetation sampling included the measurement of PAI, plant
 163 height, and phenology through non-destructive methods. The PAI is mea-
 164 sured using the notion of hemispherical digital photography. During each
 165 measurement day, we took ten photos along two transects which are sepa-
 166 rated by 2m in each sampling point, using a wide-angle lens mounted on a
 167 digital camera. All images were post-processed using the CanEYE software
 168 to provide an estimate of PAI. We have sampled the vegetation crop water
 169 content intermittently at few phenological stages. At the maturity stage,
 170 the water content in the grain was 14.2% to 19.6% (wet basis) while the
 171 stem water content got reduced by 36% to 42% (wet basis) as compared
 172 to the dough stage. The overall phenology of rice is usually expressed with
 173 three major stages: vegetative, reproductive, and mature (or ripening). The
 174 statistics of bio-physical and soil parameters are given in Table 1.

175 **3. Satellite data pre-processing**

176 We acquired RADARSAT-2 images in Fine Quad (FQ) wide mode from
 177 July to November 2018 over the test site as shown in Table 2. We then

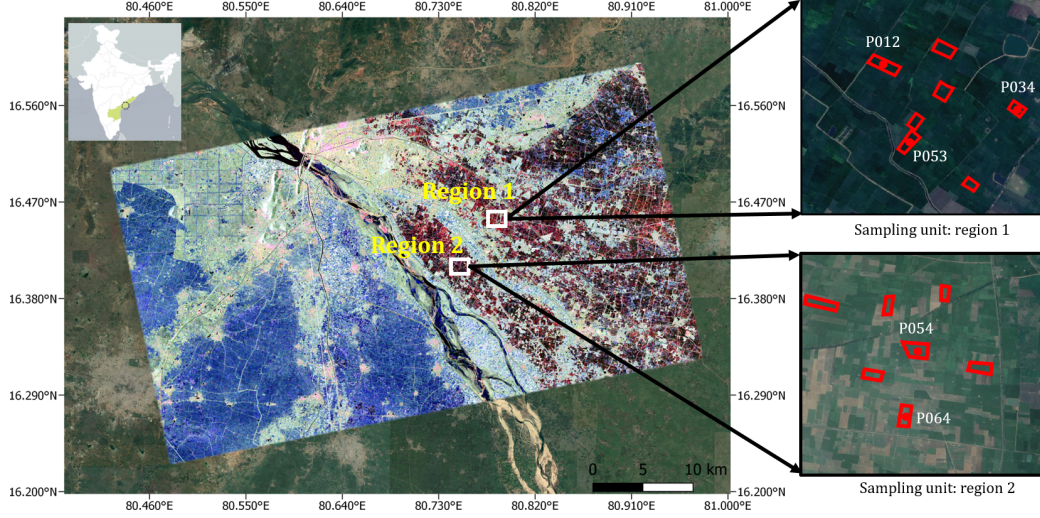


Figure 1: The Google Earth image of the JECAM test site over Vijayawada, India is overlaid with a Pauli RGB image obtained from SAR data acquired on 29 Jul 2018. The samples from region 1 and 2 are used for temporal analysis and clustering. The distribution of five in-situ data points is shown in the sampling unit of region 1 and region 2.

178 apply a multi-look factor of 2×3 pixels in the range and azimuth directions,
 179 respectively, to generate ≈ 15 m square pixel images. In general, the parcel
 180 sizes in this test area are small. However, during rice cultivation, many fields
 181 are cultivated alongside the field boundaries. Therefore, the fields seem to
 182 be quasi-homogeneous, depending on cultivation practices. Since the area is
 183 quasi-homogeneous, we apply a 3×3 boxcar filter (Lee and Pottier, 2009) to
 184 each coherency matrix (\mathbf{T}) in the images for speckle reduction. Furthermore,
 185 we generate simulated compact polarimetric (CP) SAR data from the FP
 186 data with 0° orientation angle and -45° ellipticity angle (shown in Appendix
 187 B). We co-register all FP and CP images with the $\text{RMSE} \leq 0.25$ m.

Table 2: Specification of the C-band full-pol RADARSAT-2 acquisitions over the test site during the field campaign (*az*: azimuth resolution and *rg*: range resolution)

Acquisition date	Beam mode	Incidence angle range (deg.)	Orbit	$az(m) \times rg(m)$
05/07/2018	FQ15W	33.73–36.65	Ascending	4.73×5.11
29/07/2018	FQ15W	33.73–36.65	Ascending	4.73×5.11
22/08/2018	FQ15W	33.73–36.65	Ascending	4.73×5.11
09/10/2018	FQ15W	33.73–36.65	Ascending	4.73×5.11
02/11/2018	FQ15W	33.73–36.64	Ascending	4.73×5.11
26/11/2018	FQ15W	33.73–36.64	Ascending	4.73×5.11

188 4. Methodology

189 In this section, we present the newly proposed scattering-type parameters
190 for both full- and compact-pol SAR data (Dey et al., 2020) for monitoring
191 rice crop. Alongside this, we propose an unsupervised clustering scheme
192 utilizing these new parameters along with the scattering entropy parameter
193 (i.e., a measure of randomness) derived from full (FP) and compact-pol (CP)
194 SAR data.

195 4.1. Full-polarimetry

196 In FP SAR, the 2×2 complex scattering matrix \mathbf{S} encompasses complete
197 polarimetric information about backscattering from targets for each pixel.
198 It is expressed in the backscatter alignment (BSA) convention in the linear
199 horizontal (H) and linear vertical (V) polarization basis as,

$$\mathbf{S} = \begin{bmatrix} S_{HH} & S_{HV} \\ S_{VH} & S_{VV} \end{bmatrix} \quad (1)$$

Each element of the matrix represents the backscattering response of the target at a specific polarization. The diagonal elements of the matrix represent the co-polarized scattering information, while the off-diagonal terms represent the cross-pol information. In the monostatic backscattering case, the reciprocity theorem constrains the scattering matrix to be symmetric, *i.e.*, $S_{HV} = S_{VH}$.

To reduce the speckle effect in \mathbf{S} , the multi-looked Hermitian positive semi-definite 3×3 coherency matrix \mathbf{T} is obtained from the averaged outer product of the target vector \mathbf{k}_P (derived using the Pauli basis matrix, Ψ_P) with its conjugate (Lee and Pottier, 2009).

$$\Psi_P = \left\{ \sqrt{2} \begin{bmatrix} 1 & 0 \\ 0 & 1 \end{bmatrix}, \sqrt{2} \begin{bmatrix} 1 & 0 \\ 0 & -1 \end{bmatrix}, \sqrt{2} \begin{bmatrix} 0 & 1 \\ 1 & 0 \end{bmatrix} \right\}$$

$$\mathbf{k}_P = \frac{1}{2} \text{Tr}(\mathbf{S} \Psi_P) \implies \mathbf{k}_P = \frac{1}{\sqrt{2}} [S_{HH} + S_{VV}, S_{HH} - S_{VV}, 2S_{HV}]^T$$

$$\mathbf{T} = \frac{1}{N} \sum_{i=1}^N \mathbf{k}_{Pi} \mathbf{k}_{Pi}^{*T}$$

where N denotes the square window size for spatial averaging and Tr is the sum of the diagonal elements of the matrix.

When a polarized electromagnetic (EM) wave scatters from a random mixture of targets, it becomes partially polarized. The state of polarization of a partially polarized EM wave is characterized in terms of the degree of polarization ($0 \leq m \leq 1$). The degree of polarization is defined as the ratio of the (average) intensity of the polarized portion of the wave to that of the (average) total intensity of the wave. For a completely polarized EM wave,

214 $m = 1$ and for a completely unpolarized EM wave, $m = 0$. In between these
 215 two extreme cases, the EM wave is said to be partially polarized, $0 < m < 1$.

216 Barakat (Barakat, 1977) provided an expression of m for the $N \times N$
 217 coherency matrix. This expression is used in this study to obtain the degree
 218 of polarization m_{FP} from the 3×3 coherency matrix \mathbf{T} for FP SAR data as,

$$m_{\text{FP}} = \sqrt{1 - \frac{27|\mathbf{T}|}{(\text{Tr}(\mathbf{T}))^3}}, \quad (2)$$

219 where $|\cdot|$ is the determinant of a matrix.

220 From the interpretation of the Huynen parameters in terms of certain
 221 general properties of the target geometry, it can be inferred that T_{11} is the
 222 generator of target symmetry and represents the scattered power from a
 223 regular, smooth and convex parts of the scatterer. Similarly, $(T_{22} + T_{33})$ is
 224 the generator of the target structure and represents the scattered power from
 225 an irregular, uneven and non-convex parts of the scatterer (Lee and Pottier,
 226 2009). Therefore, with respect to the total polarized scattered power (i.e.,
 227 $m_{\text{FP}}\text{Span}$) from a scatterer, let us denote,

$$\tan \eta_1 = \frac{T_{11}}{m_{\text{FP}} \text{Span}} \quad \text{and} \quad \tan \eta_2 = \frac{T_{22} + T_{33}}{m_{\text{FP}} \text{Span}}, \quad (3)$$

228 where, $T_{11} = \langle |S_{\text{HH}} + S_{\text{VV}}|^2 \rangle$, $T_{22} = \langle |S_{\text{HH}} - S_{\text{VV}}|^2 \rangle$, and $T_{33} = 4\langle |S_{\text{HV}}|^2 \rangle$ are
 229 the diagonal elements of the \mathbf{T} matrix. The total power, Span is defined in
 230 terms of the elements of the \mathbf{T} matrix as,

$$\text{Span} = T_{11} + T_{22} + T_{33}. \quad (4)$$

Here, η_1 and η_2 are two auxiliary variables representing the tangent of the ratios between the diagonal elements (T_{11} and $T_{22} + T_{33}$) of the coherency matrix, \mathbf{T} , and the total polarized scattering power ($m_{\text{FP}} \text{Span}$).

We define:

$$\tan \gamma_{\text{FP}} = \tan (\eta_1 - \eta_2), \quad (5)$$

where γ_{FP} can be related to the average scattering-type parameter, Cloude $\bar{\alpha} \in [0^\circ, 90^\circ]$ (Cloude and Pottier, 1997). However, in order to compare the two parameters within the same range, they are suitably modified as, $\hat{\alpha} = 90^\circ - 2\bar{\alpha}$ and $\theta_{\text{FP}} = 2\gamma_{\text{FP}}$, which is a roll-invariant parameter (detailed in Appendix A.1) is given as,

$$\theta_{\text{FP}} = 2 \tan^{-1} \left(\frac{m_{\text{FP}} \text{Span} (T_{11} - T_{22} - T_{33})}{T_{11} (T_{22} + T_{33}) + m_{\text{FP}}^2 \text{Span}^2} \right) \in [-90^\circ, 90^\circ]. \quad (6)$$

It can be noticed from equation (6) that when $T_{11} = 0$ and $m_{\text{FP}} = 1$, then $\text{Span} = T_{22} + T_{33}$ and $\theta_{\text{FP}} = -90^\circ$. Similarly, when $T_{22} + T_{33} = 0$ and $m_{\text{FP}} = 1$, then $\text{Span} = T_{11}$ and $\theta_{\text{FP}} = 90^\circ$. Besides, as θ_{FP} approaches 0, scattering randomness increases and at $\theta_{\text{FP}} = 0^\circ$, the scattering is purely random (or depolarized).

The eigen-decomposition of \mathbf{T} can be expressed as,

$$\mathbf{T} = \mathbf{U}_3 \mathbf{\Sigma} \mathbf{U}_3^{-1} \quad (7)$$

where $\mathbf{\Sigma}$ is the 3×3 diagonal matrix with non-negative elements, $\lambda_1 \geq \lambda_2 \geq \lambda_3 \geq 0$, which are the eigenvalues of \mathbf{T} . The pseudo probabilities, p_i obtained

from the eigenvalues are defined as,

$$p_i = \frac{\lambda_i}{\sum_{k=1}^3 \lambda_k}, \quad (8)$$

which are then used to define the scattering entropy (Lee and Pottier, 2009)

as,

$$H_{\text{FP}} = -\sum_{k=1}^3 p_k \log_3(p_k), \quad (9)$$

However, in this study, we use the quantity $\overline{H}_{\text{FP}} = 1 - H_{\text{FP}}$ in the $\overline{H}_{\text{FP}}/\theta_{\text{FP}}$ polar plot as shown in figure 2. The feasible regions in the $\overline{H}_{\text{FP}}/\theta_{\text{FP}}$ polar

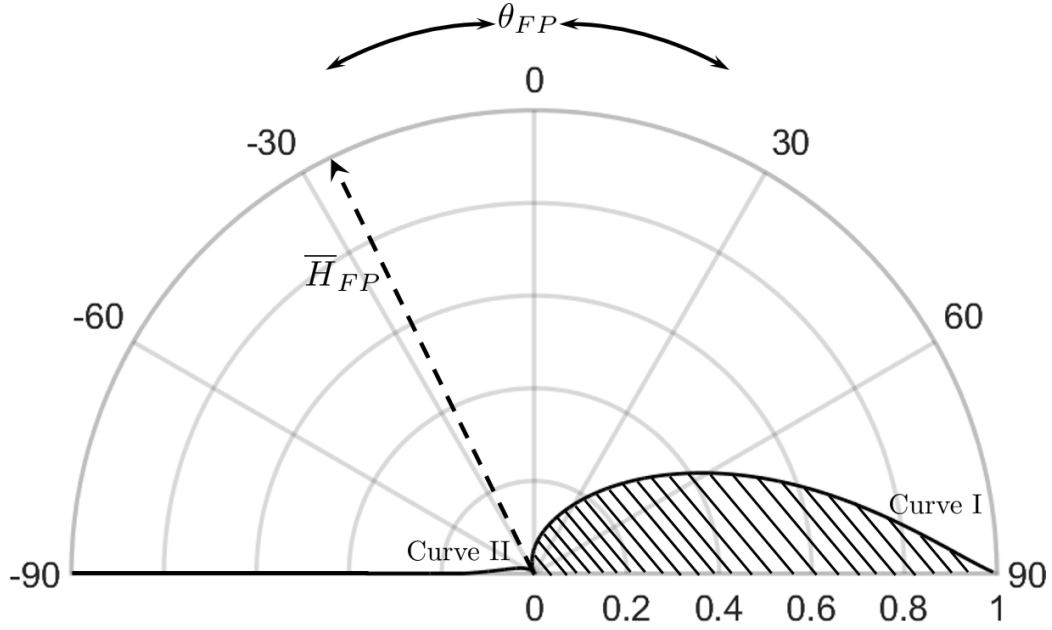


Figure 2: The $\overline{H}_{\text{FP}}/\theta_{\text{FP}}$ plane displayed in polar plot. Curve I and Curve II represent the azimuthal symmetry lines. No scattering mechanisms exist in the shaded portion of the plane.

253 plot is represented by two bounding curves, Curve I and Curve II in figure 2.

$$\text{Curve I, } [\mathbf{T}]_I = \begin{bmatrix} 1 & 0 & 0 \\ 0 & m & 0 \\ 0 & 0 & m \end{bmatrix} \quad 0 \leq m \leq 1 \quad (10)$$

$$\text{Curve II, } [\mathbf{T}]_{II} = \begin{bmatrix} 2m-1 & 0 & 0 \\ 0 & 1 & 0 \\ 0 & 0 & 1 \end{bmatrix} \quad 0.5 \leq m \leq 1 \quad (11)$$

254 4.2. Compact-polarimetry

255 The CP mode measures a projection of the 2×2 complex scattering
256 matrix \mathbf{S} as,

$$\begin{aligned} \begin{bmatrix} E_{CH} \\ E_{CV} \end{bmatrix} &= \frac{1}{\sqrt{2}} \begin{bmatrix} S_{HH} & S_{HV} \\ S_{VH} & S_{VV} \end{bmatrix} \begin{bmatrix} 1 \\ \pm i \end{bmatrix} \\ &= \frac{1}{\sqrt{2}} \begin{bmatrix} S_{HH} \pm iS_{HV} \\ S_{VH} \pm iS_{VV} \end{bmatrix} \end{aligned} \quad (12)$$

257 where the subscript C can be either the left-hand circular (L) transmit with
258 a $+$ sign or the right-hand circular (R) transmit with a $-$ sign. The 2×2
259 covariance matrix is then obtained from the elements of the scattering vector
260 as,

$$\mathbf{C}_2 = \begin{bmatrix} \langle |E_{CH}|^2 \rangle & \langle E_{CH} E_{CV}^* \rangle \\ \langle E_{CV} E_{CH}^* \rangle & \langle |E_{CV}|^2 \rangle \end{bmatrix}. \quad (13)$$

261 For CP-SAR data, the 4×1 Stokes vector $\vec{\mathbf{g}}$ can be written in terms of

262 the elements of the 2×2 covariance matrix \mathbf{C}_2 as,

$$\mathbf{g}_i = \begin{bmatrix} g_0 \\ g_1 \\ g_2 \\ g_3 \end{bmatrix} = \begin{bmatrix} C_{11} + C_{22} \\ C_{11} - C_{22} \\ C_{12} + C_{21} \\ \pm j (C_{12} - C_{21}) \end{bmatrix}, \quad (14)$$

263 where \pm corresponds to left and right circular polarization respectively.

264 From the elements of $\vec{\mathbf{g}}$, the backscatter power in the same sense ($SC =$
 265 $\frac{g_0 - g_3}{2}$) and opposite sense ($OC = \frac{g_0 + g_3}{2}$) to the transmitted circular po-
 266 larization is utilized to derive the scattering-type parameter for the compact-
 267 polarimetric SAR data similar to the FP case. Here, OC is the generator of
 268 target symmetry and represents the scattered power from a regular, smooth
 269 and convex parts of the scatterer. Similarly, SC is the generator of the target
 270 structure and represents the scattered power from an irregular, uneven and
 271 non-convex parts of the scatterer:

$$\tan \zeta_1 = \frac{OC}{m_{CP} \text{Span}}, \quad \text{and} \quad \tan \zeta_2 = \frac{SC}{m_{CP} \text{Span}} \quad (15)$$

272 where the total power Span is defined as,

$$\text{Span} = SC + OC \quad (16)$$

273 Here, ζ_1 and ζ_2 are two auxiliary variables representing the tangent of the
 274 ratios between the opposite and same sense circular polarized backscatter
 275 powers (OC and SC) and the total polarized scattering power ($m_{CP} \text{Span}$).

276 Similar to FP, we define:

$$\tan \gamma_{\text{CP}} = \tan (\zeta_1 - \zeta_2) \quad (17)$$

277 where γ_{CP} can be analogously related to the polarization ellipticity parameter
 278 $\chi \in [-45^\circ, 45^\circ]$. However, in order to compare, the two parameters within
 279 the same range, they are suitably scaled as, $\bar{\chi} = -2\chi$ and $\theta_{\text{CP}} = 2\gamma_{\text{CP}}$ which
 280 is a roll-invariant parameter (detailed in Appendix A.2) is given as,

$$\theta_{\text{CP}} = 2 \tan^{-1} \left(\frac{m_{\text{CP}} \text{Span}(OC - SC)}{OC \times SC + m_{\text{CP}}^2 \text{Span}^2} \right) \in [-90^\circ, 90^\circ] \quad (18)$$

281 Similar to θ_{FP} , it can be noticed from (18) that for a pure dihedral scat-
 282 terer, i.e., when $OC = 0$ and $m_{\text{CP}} = 1$, then $\text{Span} = SC$ and $\theta_{\text{CP}} = -90^\circ$.
 283 Similarly, for a pure trihedral scatterer, i.e., when $SC = 0$ and $m_{\text{CP}} = 1$,
 284 then $\text{Span} = OC$ and $\theta_{\text{CP}} = 90^\circ$. Besides, as θ_{CP} approaches 0, scattering
 285 randomness increases and at $\theta_{\text{CP}} = 0^\circ$, the scattering is purely random (or
 286 depolarized).

287 The expression for the Barakat degree of polarization for the compact-
 288 polarimetric case is given as,

$$m_{\text{CP}} = \sqrt{1 - \frac{4|\mathbf{C}_2|}{(\text{Tr}(\mathbf{C}_2))^2}}. \quad (19)$$

289 The eigen-decomposition of \mathbf{C}_2 can be expressed as,

$$\mathbf{C}_2 = \mathbf{U}_2 \mathbf{\Sigma} \mathbf{U}_2^{-1}, \quad (20)$$

where $\mathbf{\Sigma}$ is a 2×2 diagonal matrix with non-negative elements, $\lambda_1 \geq \lambda_2 \geq 0$, which are the eigenvalues of \mathbf{C}_2 . The pseudo probabilities, p_i obtained from the eigenvalues are defined as,

$$p_i = \frac{\lambda_i}{\sum_{k=1}^2 \lambda_k}, \quad (21)$$

which are then used to define the scattering entropy (H_{CP}) for CP-SAR data as,

$$H_{CP} = -\sum_{k=1}^2 p_k \log_2(p_k). \quad (22)$$

As mentioned earlier for the FP case, we use the quantity $\overline{H}_{CP} = 1 - H_{CP}$ in the $\overline{H}_{CP}/\theta_{CP}$ polar plot as shown in figure 3. Similar to FP, the feasible

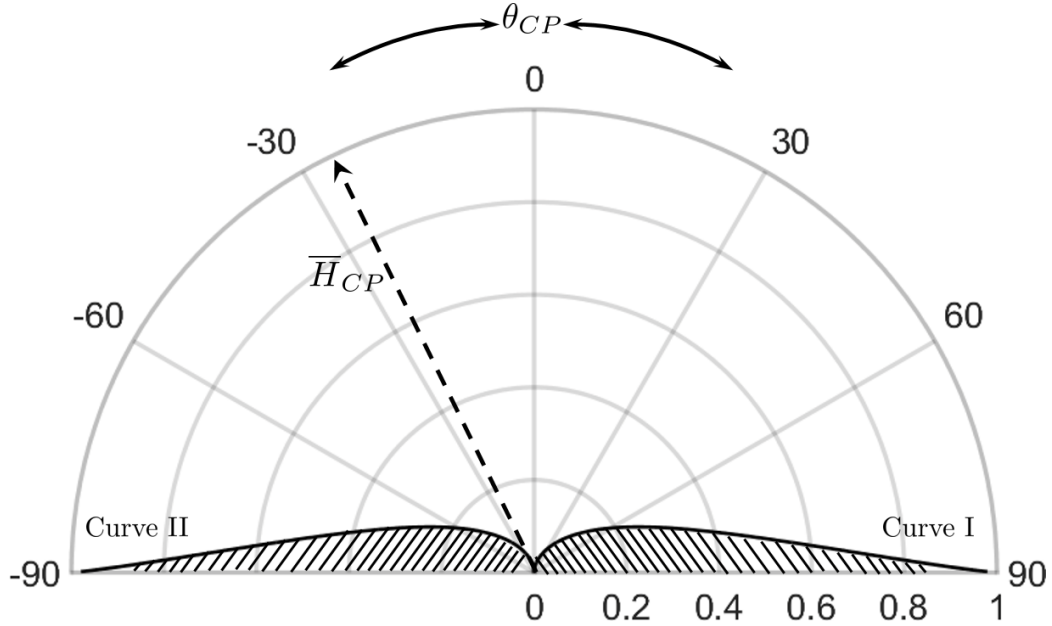


Figure 3: The $\overline{H}_{CP}/\theta_{CP}$ plane displayed in polar plot. Curve I and Curve II represent the azimuthal symmetry lines. No scattering mechanisms exist in the shaded portion of the plane.

regions in the $\overline{H}_{\text{CP}}/\theta_{\text{CP}}$ polar plot is represented by two bounding curves,
Curve I and Curve II in figure 3.

$$\text{Curve I, } [\mathbf{C}]_I = \begin{bmatrix} \frac{2m+1}{4} & i\frac{2m-1}{4} \\ -i\frac{2m-1}{4} & \frac{2m+1}{4} \end{bmatrix} \quad 0 \leq m \leq 0.5 \quad (23)$$

$$\text{Curve II, } [\mathbf{C}]_{II} = \begin{bmatrix} \frac{2m+1}{4} & -i\frac{2m-1}{4} \\ i\frac{2m-1}{4} & \frac{2m+1}{4} \end{bmatrix} \quad 0 \leq m \leq 0.5 \quad (24)$$

4.3. Clustering

In this study, we propose clustering schemes equivalently for both FP and CP SAR data by utilizing the 2D $\overline{H}_{\text{FP}}/\theta_{\text{FP}}$ and $\overline{H}_{\text{CP}}/\theta_{\text{CP}}$ planes respectively. Besides, the zones and the boundaries of both the clustering planes are identical. From analysis with scattering model (random volume model), it has been observed that the scattering-type from vegetation lies approximately in the range -10° to 20° (Antropov et al., 2011). The upper bound for multiple scattering ($\theta_X = 20^\circ$, where the subscript X refers to either FP or CP) is characterized by equal contributions from the ensemble of horizontal and vertical dipole scattering components from vegetation structure. In contrast, the lower bound ($\theta_X = -10^\circ$) is the characteristic of multiple scattering phenomena predominantly described by vertical vegetation structure. Hence, this region is subdivided for multiple scattering mechanisms. Unlike the $H/\overline{\alpha}$ plane, the proposed clustering scheme divides the plane into twelve zones. The scattering-type parameter θ_X divides the $\overline{H}_X - \theta_X$ plane into four sub-planes (P1:(Z1, Z2, Z3); P2:(Z4, Z5, Z6); P3:(Z7, Z8, Z9); P4:(Z10, Z11, Z12)) which consists of (1) pure even-bounce scattering (-90° to -10°) in P1; (2) even-bounce with multiple scattering (-10° to 0°) in P2; (3) odd-bounce

317 with multiple scattering (0° to 20°) in P3; (4) pure odd-bounce scattering
 318 (20° to 90°) in P4. The quantity $\bar{H}_X = 1 - H$ divides the plane into (1) high
 319 entropy (0 to 0.3); (2) medium entropy (0.3 to 0.5); (3) low entropy (0.5 to
 320 1). The $H/\bar{\alpha}$ and the \bar{H}_X/θ_X clustering plane along with the zones are given
 in figure 4. Target characterization parameters extraction and the clustering

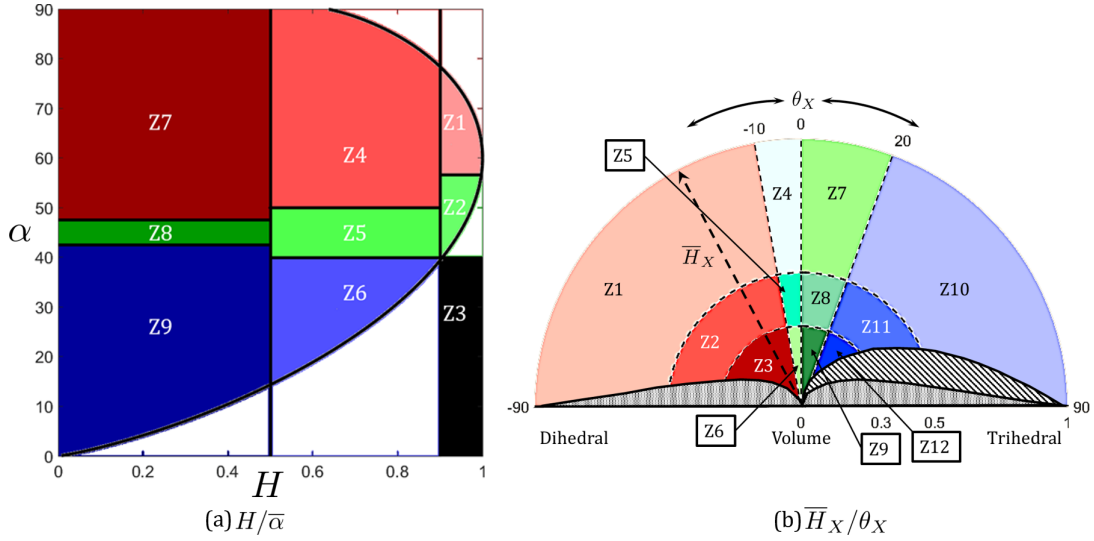


Figure 4: (a) $H/\bar{\alpha}$ clustering plane for FP SAR data with 8 clusters and (b) \bar{H}_X/θ_X clustering plane for both FP and CP SAR data with 12 clusters. Two half-circles at 0.3 and 0.5 divide \bar{H}_X into high, medium and low entropy regions while -90° to -10° represents even bounce scattering, -10° to 20° represents multiple bounce scattering and 20° to 90° represents odd bounce scattering. No scattering mechanisms exist in the shaded portion of the plane for both the FP and CP modes.

321

322 framework are implemented using MATLAB R2019b environment (the steps
 323 along with a flowchart are detailed in Appendix C). The proposed cluster-
 324 ing framework is analyzed for the C-band San-Francisco RADARSAT-2 SAR
 325 data and further utilized for phenology clustering of rice.

326 5. Results and Discussion

327 In this section, we analyze the proposed clustering framework using the
 328 C-band San-Francisco RADARSAT-2 SAR data. Following this, we perform
 329 a detailed case study for the unsupervised clustering of rice phenology over
 330 Vijayawada, India.

331 5.1. Analysis of the novel clustering framework

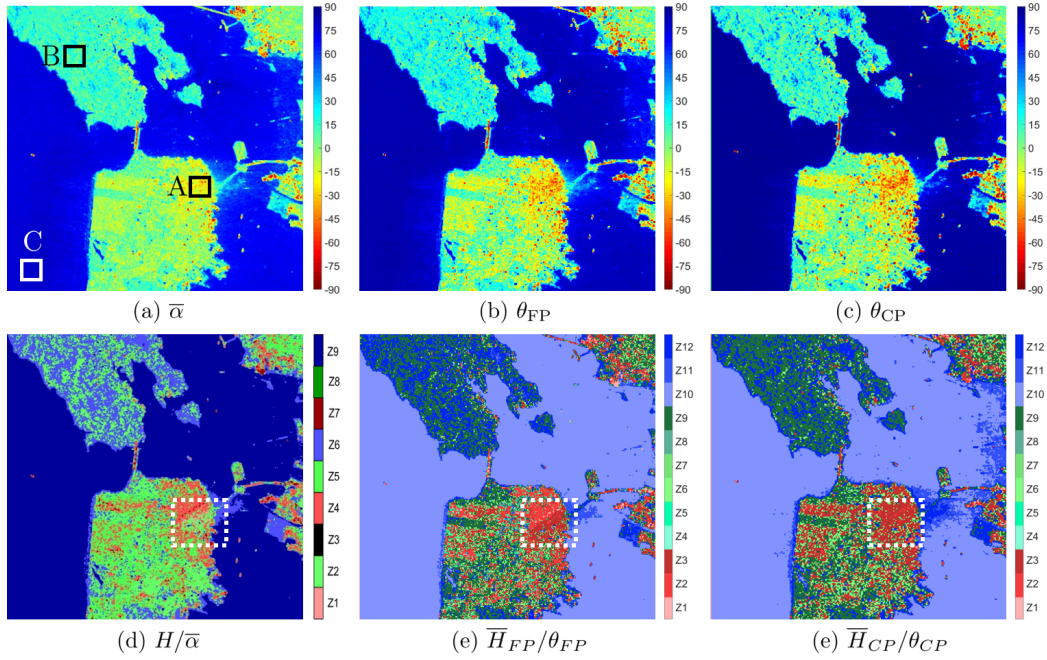


Figure 5: The scattering type parameters, $\bar{\alpha}$, θ_{FP} , θ_{CP} and the $H/\bar{\alpha}$, \bar{H}_{FP}/θ_{FP} , \bar{H}_{CP}/θ_{CP} clustered image of San Francisco Bay, USA using C-band RADARSAT-2 SAR data. Region A represents the oriented urban area, region B and C represents forest and ocean areas, respectively. The white box shows the oriented urban area where the major change during clustering occurred. $H/\bar{\alpha}$ identified it as scattering from vegetation while \bar{H}_{FP}/θ_{FP} and \bar{H}_{CP}/θ_{CP} correctly identified it as scattering from urban region.

332 The difference between the geometrical structures of the $H/\bar{\alpha}$ and \bar{H}_{FP}/θ_{FP}
 333 2D clustering planes can be observed in figure 4. As stated earlier, it may

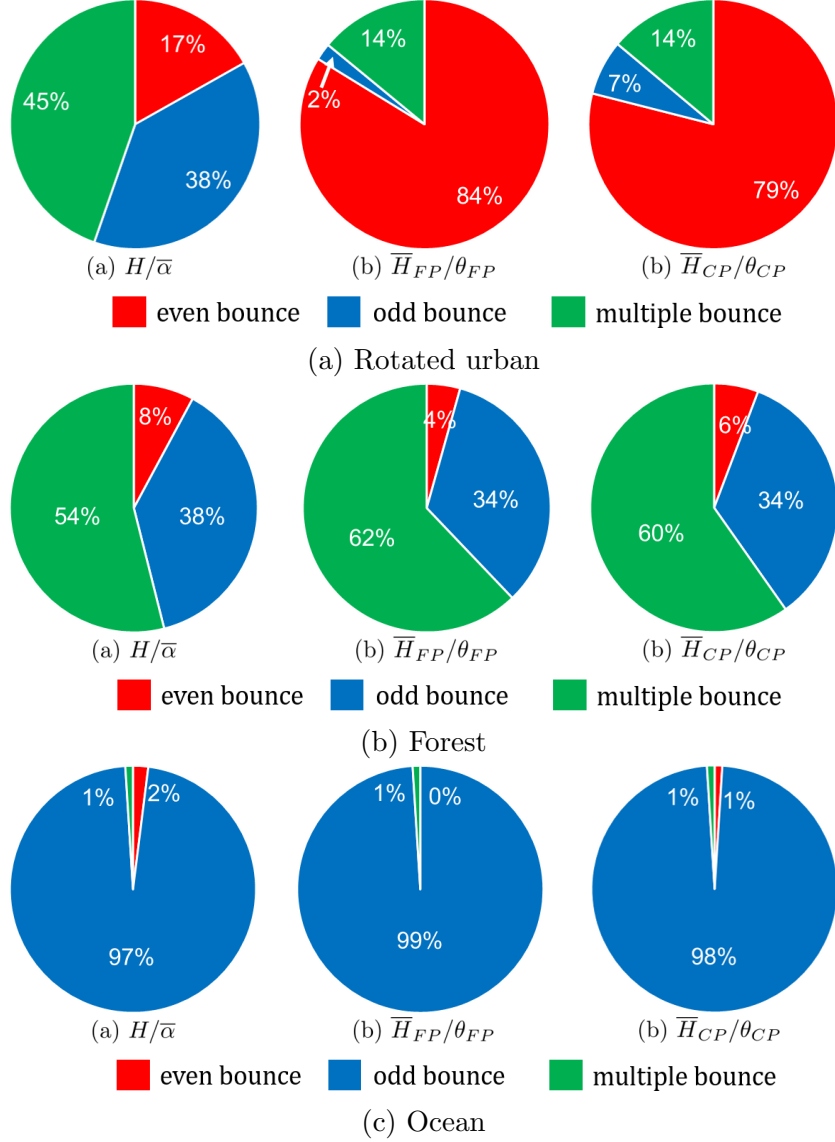


Figure 6: A comparison of the percentages of even, odd and multiple bounce scattering over (a) rotated urban, (b) forest and (c) ocean surfaces for the C-band RADARSAT-2 San Francisco Bay area image using $H/\bar{\alpha}$, \bar{H}_{FP}/θ_{FP} and \bar{H}_{CP}/θ_{CP} clustering techniques.

334 be noted that the parameter $\bar{\alpha}$ is scaled to $\hat{\alpha} = 90^\circ - 2\bar{\alpha}$ solely for the
335 sake of qualitative comparison. The ability of the two clustering planes, i.e.,

336 $\overline{H}_{\text{FP}}/\theta_{\text{FP}}$ and $\overline{H}_{\text{CP}}/\theta_{\text{CP}}$ to classify different land-cover classes is apparent in
 337 this figure. Region A, B and C in figure 5 are respectively the oriented urban
 338 area, forest area and ocean areas. The dashed white box in figure 5 high-
 339 lights distinct changes in the scattering types as well as the clustering zones
 340 for differently oriented targets.

341 It can be observed from figure 6 that in the $H/\overline{\alpha}$ plane, the even-bounce
 342 scattering mechanism over oriented urban area (A) is only 17 % while the
 343 odd-bounce and multiple-bounce scattering mechanism are 38 % and 45 %, respectively.
 344 In contrast, the contribution of even-bounce dominant scatter-
 345 ing mechanism in $\overline{H}_{\text{FP}}/\theta_{\text{FP}}$ and $\overline{H}_{\text{CP}}/\theta_{\text{CP}}$ are 84 % and 79 %, respectively.
 346 On the other hand, over the forest area (B), the multiple-bounce scatter-
 347 ing mechanism is 8 % higher for $\overline{H}_{\text{FP}}/\theta_{\text{FP}}$ and 6 % higher for $\overline{H}_{\text{CP}}/\theta_{\text{CP}}$ as
 348 compared to $H/\overline{\alpha}$. Similarly, over the ocean area (C) the odd-bounce scat-
 349 tering mechanism has increased marginally by 2 % and 1 % for $\overline{H}_{\text{FP}}/\theta_{\text{FP}}$ and
 350 $\overline{H}_{\text{CP}}/\theta_{\text{CP}}$, respectively.

351 This suggests that the discriminating ability of $\overline{H}_{\text{FP}}/\theta_{\text{FP}}$ and $\overline{H}_{\text{CP}}/\theta_{\text{CP}}$
 352 scheme is by and large higher than $H/\overline{\alpha}$. This marked ability might be due
 353 to 1) the joint utilization of the Barakat degree of polarization along with
 354 essential information from elements of the coherency matrix in deriving the
 355 scattering-type parameters, 2) the notion of an extended clustering procedure
 356 (i.e., 12 clusters) using entropy and the scattering-type parameters. Hence,
 357 we use the proposed clustering schemes with θ_{FP} and θ_{CP} , for the temporal
 358 analysis of two different varieties of rice crops over Vijayawada, India using
 359 FP RADARSAT-2 data and simulated CP SAR data. In this study, we
 360 analyze the phenological changes of rice using these parameters and the new

361 clustering scheme.

362 5.2. Temporal variations of θ_X and \overline{H}_X/θ_X clustering planes for rice

363 In this section, we discuss the temporal analysis of θ_{FP} and θ_{CP} along with
364 phenology clustering of rice in the $\overline{H}_{\text{FP}}/\theta_{\text{FP}}$ and $\overline{H}_{\text{CP}}/\theta_{\text{CP}}$ polar plane. The
365 temporal variation of θ_{FP} and θ_{CP} for FP and CP SAR data, respectively, are
366 shown in figure 7. Both qualitative and quantitative analyses of the temporal
367 variations in θ_{FP} and θ_{CP} utilizing data from five in-situ points (viz., P012,
368 P054, P064, P034, and P053) are shown in figure 8. Besides, the $\overline{H}_{\text{FP}}/\theta_{\text{FP}}$ and
369 $\overline{H}_{\text{CP}}/\theta_{\text{CP}}$ planes are divided into 12 zones based on different scattering-type
370 information. In figure 4, zones (Z1, Z2, Z3), (Z10, Z11, Z12), and (Z4, Z5, Z6,
371 Z7, Z8, Z9) represent even, odd and multiple scattering types respectively.
372 In this study, these clustering zones (figure 16) are utilized to monitor the
373 growth stages of rice using full and simulated compact polartimetric SAR
374 data. The temporal variations of the clusters are shown in figures 9 to 14.

375 In figure 9a and figure 9b, the θ_{FP} and θ_{CP} values are majorly within the
376 odd-bounce scattering region on 05 Jul depending on soil surface condition.
377 Although the overall values of θ_{FP} and θ_{CP} are comparable, the FP image
378 can better capture the subtle variations over the land cover compared to the
379 CP image. During this period, the field condition differs depending on the
380 ploughed and non-ploughed situation. The comparatively low values ($\leq 90^\circ$)
381 for θ_{FP} and θ_{CP} are likely due to soil roughness as compared to the incident 5.6
382 cm C-band wavelength (Mandal et al., 2020). Hence, dense clusters are seen
383 in Z10, Z11, and Z12, which corresponds respectively to low entropy even-
384 bounce scattering, medium entropy even-bounce scattering, and high entropy
385 even-bounce scattering regions. Moreover, a few data points lying in region

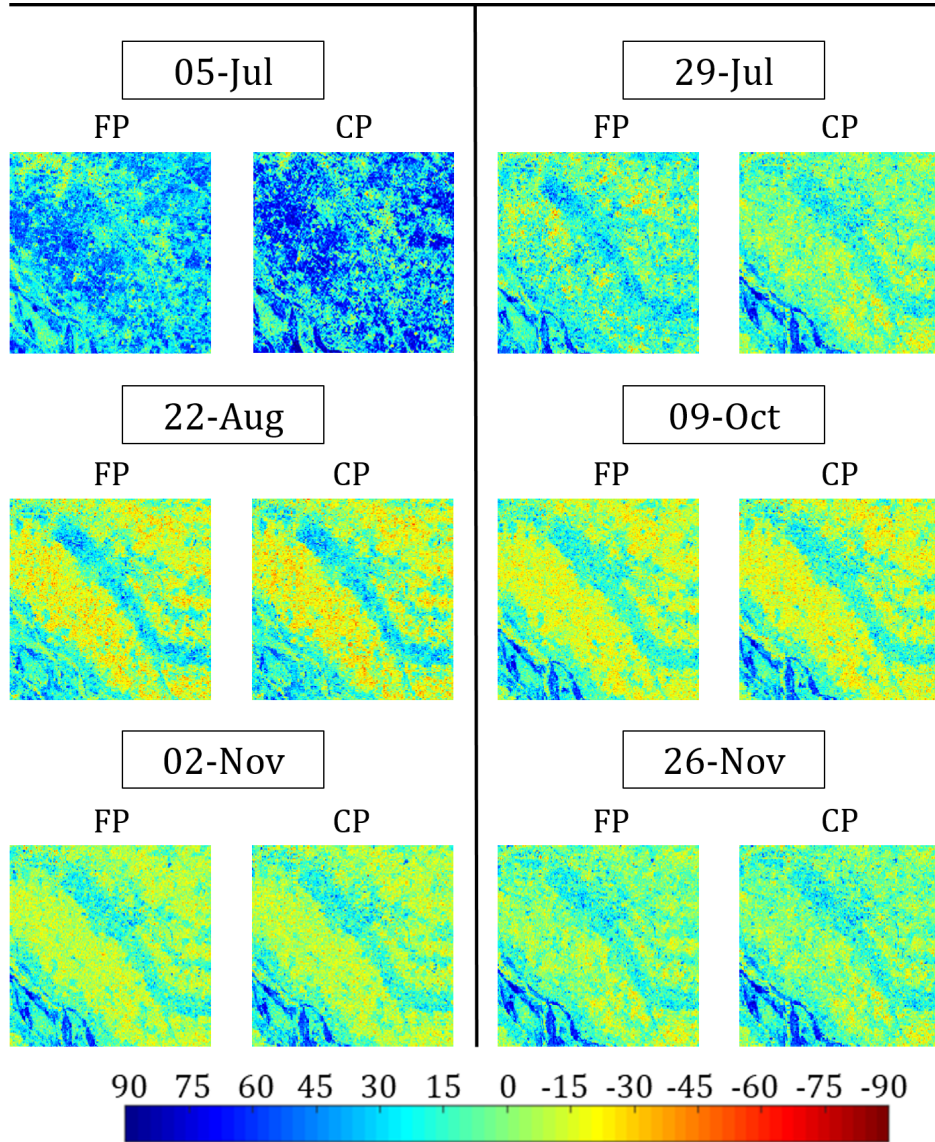


Figure 7: Variation of θ_{FP} and θ_{CP} images for FP and CP over the study area. The growth stages are: 5-Jul: Bare field, 29-Jul: Early tillering, 22-Aug: Advanced tillering, 9-Oct: Flowering, 2-Nov: Early dough, and 26-Nov: Maturity

386 Z3 is due to the early transplantation stage. Besides, tillage operation in
 387 some fields has produced soil surface roughness, which increased the entropy,

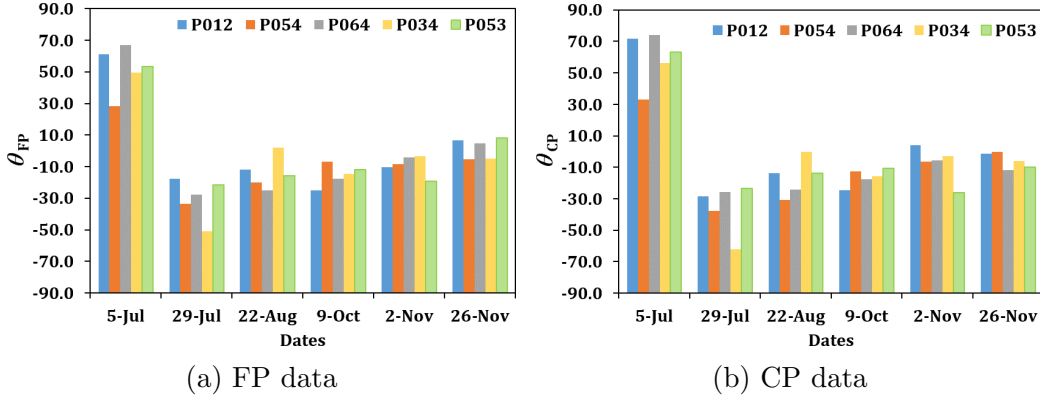


Figure 8: Temporal variation of θ_{FP} and θ_{CP} for rice using FP and CP data for five in-situ points: P012, P054, P064, P034, and P053. The growth stages are: 5-Jul: Bare field, 29-Jul: Early tillering, 22-Aug: Advanced tillering, 9-Oct: Flowering, 2-Nov: Early dough, and 26-Nov: Maturity

and hence, a sparse cluster can also be seen in Z9 and Z6. The proportion of pixels over different scattering regions at each phenological stage is shown in Table 3 and figure 16. High odd bounce scattering (86.26 %) was noted for FP data. Besides, due to the slight roughness a small component of multiple bounce scattering (12.24 %) is observed during this period, whereas even bounce scattering contribution was only 0.90 %.

A significant change in the data cluster is seen on 29 Jul (figure 10a and figure 10b). During this period, most of the rice fields were in the early tillering stage, while other non-cultivated fields had moist soil with high roughness that is evident from in-situ data. During this period, variation of θ_{FP} is -17° to -51° while θ_{CP} ranges from -23° to -62° as seen in figure 8. Also, this highly rough soil surface during this period has generated a high degree of randomness in the received EM wave, which resulted in an increased entropy. Hence, a shift from low entropy zone (Z10) to high (Z12) and medium (Z11) entropy zones is evident on 29 Jul. Also, some data

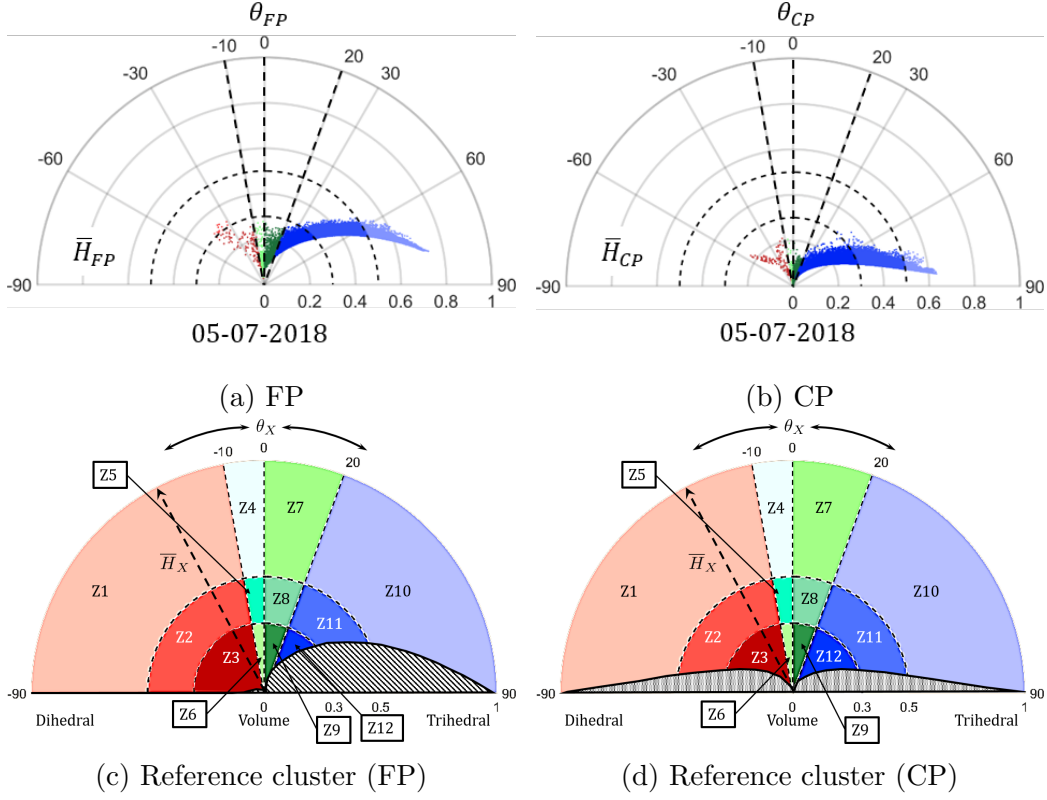


Figure 9: The \bar{H}_X/θ_X scatter plane for rice using FP and CP SAR data on 05-Jul.

points in zones Z11 and Z12 are $\theta_{FP} \leq 30^\circ$, which is due to the scattering from the water surface in the rice fields (Lopez-Sanchez et al., 2014). However, compared to θ_{FP} , the values of θ_{CP} are 5° to 10° higher in this period.

The density of the data points in Z6 and Z9 zones has also increased on 29 Jul, while rice transplantation was undergoing in some other fields. Therefore, a moderately high accumulation of data points can also be seen in Z3 (figure 10a and figure 10b). Moreover, the previously sown rice fields had achieved a higher vegetative stage due to which the areal coverage by the crop canopy had increased, thereby slightly decreasing the scattering entropy.

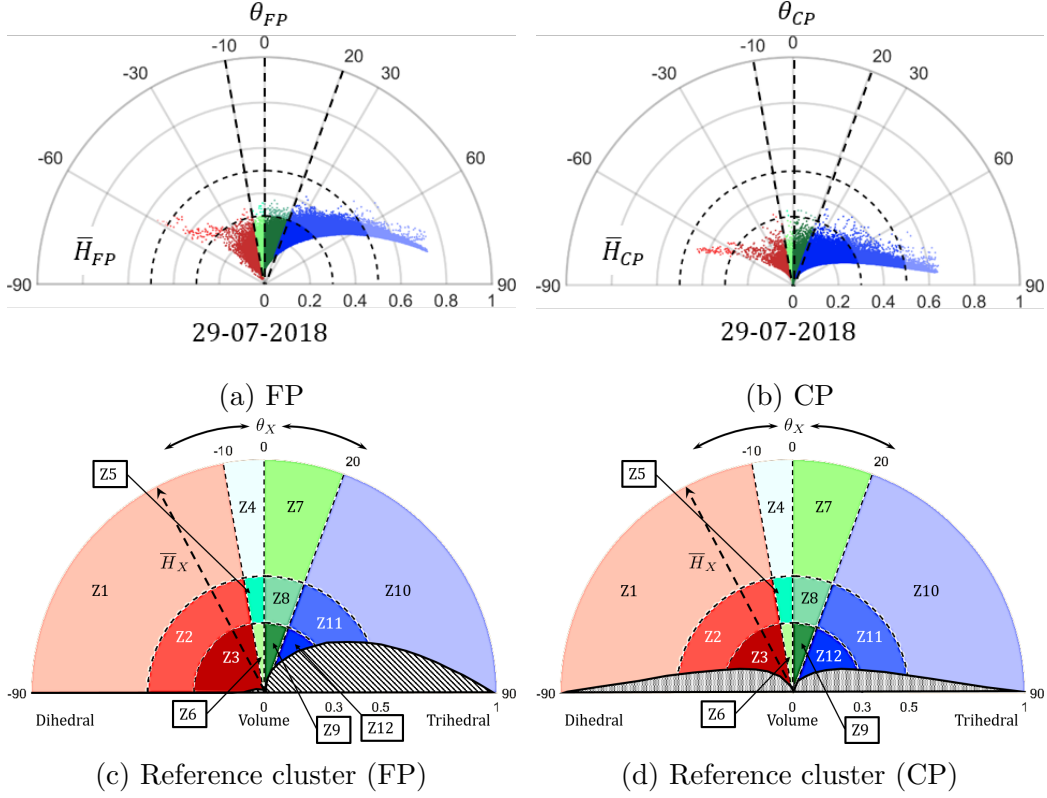


Figure 10: The \bar{H}_X/θ_X scatter plane for rice using FP and CP SAR data on 29-Jul.

Due to this aspect, a few data points are sparsely clustered in the Z2 region on 29 Jul. Furthermore, in zones Z2 and Z3, the values of θ_{CP} is 2° to 5° higher than θ_{FP} . Hence, the even bounce scattering had increased by 75.89% and multiple scattering had increased by 16.49%. A noteworthy decrease in the odd bounce scattering (82.38%) is observed which is most likely due to the increase of double-bounce for the presence of stems, which also helps to reduce the surface roughness and the contribution from the ground.

On 22 Aug, dense clusters can be seen in Z3 for FP and CP data (figure 11a and figure 11b), which is due to the tillering stage of rice. Dur-

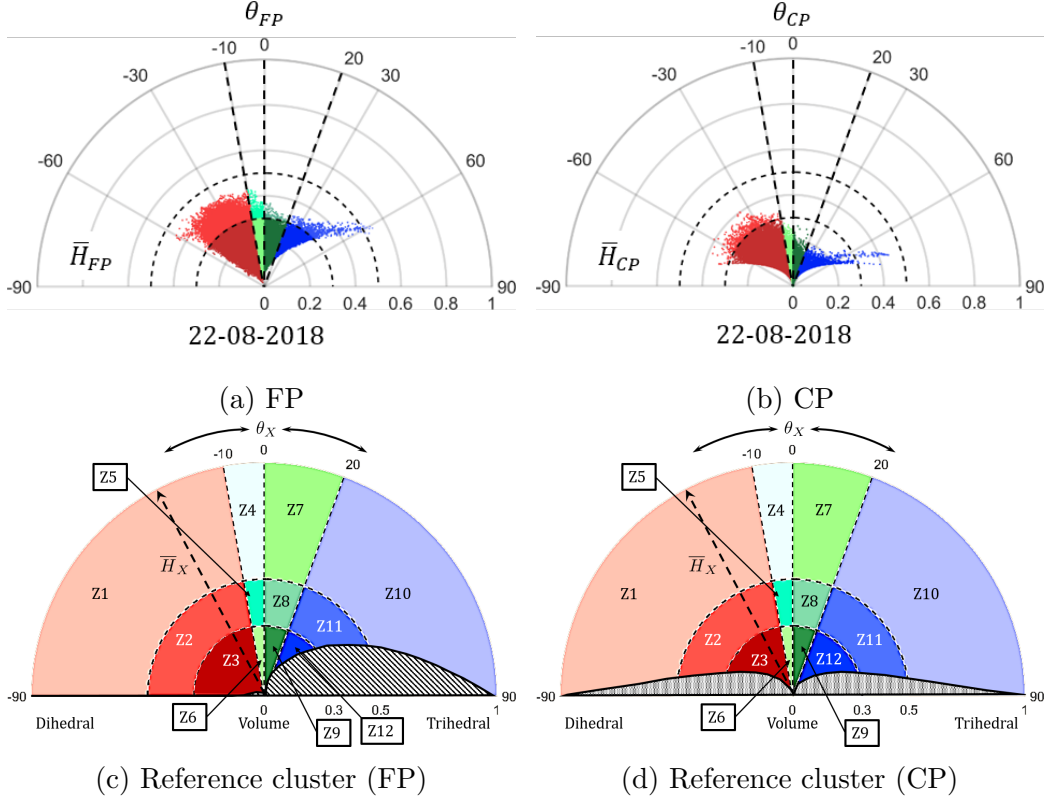


Figure 11: The \bar{H}_X/θ_X scatter plane for rice using FP and CP SAR data on 22-Aug.

ing this stage, the fields are flooded with water, and the stems are almost
 vertical, which acts as dihedral scatterers and generates even-bounce scat-
 tering (Yonezawa et al., 2012). Hence, a significant shift in the scattering
 mechanism from odd-bounce to even-bounce is visible during 22 Aug. During
 this period, \bar{H}_{CP} is lower than \bar{H}_{FP} , which might be due to less polarimetric
 information content. Similar to 29 Jul, θ_{CP} is higher than θ_{FP} at this time.
 Additionally, due to the variation in the θ_{CP} and H_{CP} values according to
 crop morphology, significant change among Z5, Z6, Z8, and Z9 zones can
 be observed compared to 29 Jul. Also, we observe an increasing trend in

430 the plots in figure 8 due to the reduction in even-bounce multiple scattering.
 431 Besides, the orientation, shape, and size of each crop were not the same, and
 432 hence there was also a possibility of rough soil surface stretching out from the
 433 water surface. Therefore, these phenomena could induce high randomness in
 434 the scattered EM wave. Besides, similar to 29 Jul, some fields progressed to a
 435 higher vegetative stage due to which a cluster can be seen in Z2. Furthermore,
 436 fields that reached the booting stage display even-bounce multiple scattering
 437 due to which the even bounce scattering power had decreased by 11.19%,
 438 while multiple bounce scattering had marginally increased by 3.67%.

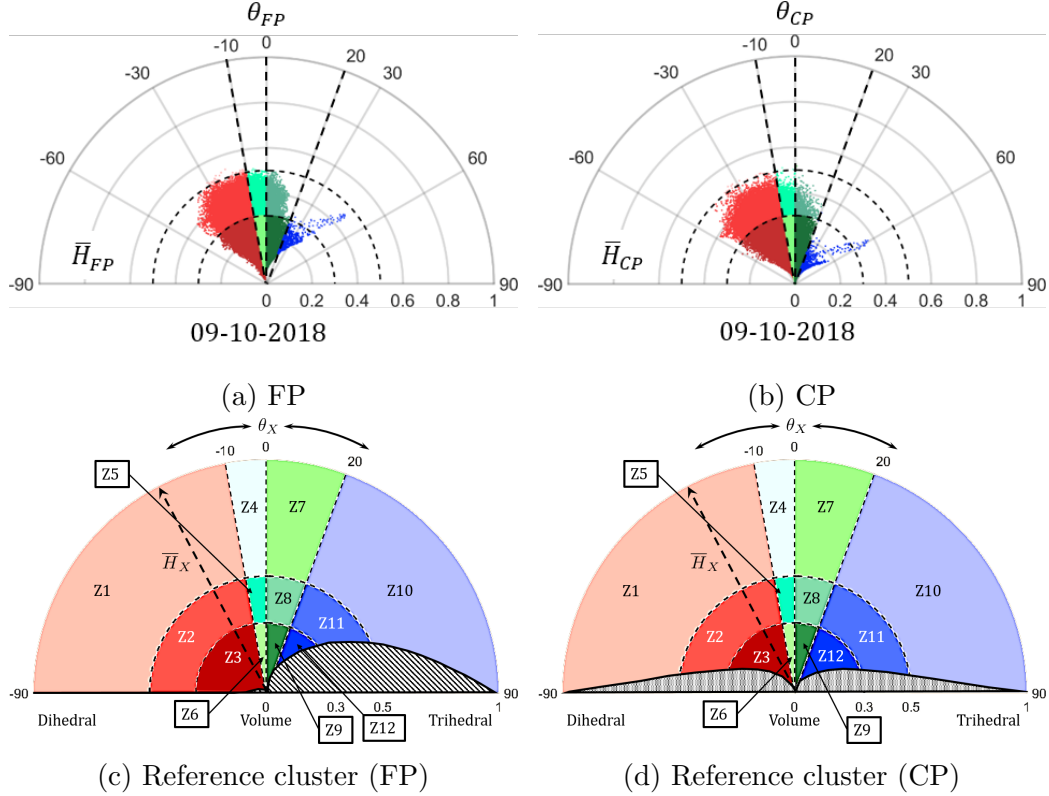


Figure 12: The \bar{H}_X/θ_X scatter plane for rice using FP and CP SAR data on 09-Oct.

439 On 09 Oct, both $\overline{H}_{\text{FP}}/\theta_{\text{FP}}$ and $\overline{H}_{\text{CP}}/\theta_{\text{CP}}$ planes show a shift towards
 440 the medium entropy region (i.e., Z2 and Z5 zones) which is evident in fig-
 441 ure 12a and figure 12b. During this period, most of the rice fields were in
 442 the inflorescence emergence stage, with θ_{FP} and θ_{CP} indicating even-bounce
 443 and even-bounce multiple scatterings. Moreover, the amount of cross-pol
 444 components has increased during this period and the coherence between the
 445 co-polarized channels decreased significantly. A similar type of increase in
 446 cross-pol components from transplantation to maturity stages was reported
 447 by He et al. (2018). The shift towards the Z2 and Z5 zones indicates an
 448 even-bounce scattering mechanism of the scattered EM wave. Such a re-
 449 sponse might be due to the extinction of the vertical polarization due to the
 450 canopy structure. Also, the amount of odd-bounce scattering reduced during
 451 this period, and rice foliage generated moderate odd-bounce multiple scatter-
 452 ing due to which dense cluster in the Z8 zone is noticed. The contribution of
 453 multiple bounce scattering was 40.02 % due to the full-grown rice crop with
 454 differently oriented stem, leaf structures and flowers.

455 Around 02 Nov, the rice fields reached the early dough stage, during
 456 which, the milky white substance begins to accumulate in rice panicle. Si-
 457 multaneously, the crop water content during this period remains very high,
 458 while leaf and stem produce overall complex canopy structure, which leads
 459 to high randomness in the SAR backscatter. Due to this fact, the values
 460 of \overline{H}_{FP} and \overline{H}_{CP} are low. Moreover, at this point, the clusters in Z3 and
 461 Z2 zones are due to the scattering from compound leaf and stem structure
 462 (figure 13a and figure 13b). In contrast, clusters in Z6, Z5, Z8, and Z9 zones
 463 are due to multiple scattering contribution from the intermediate complex

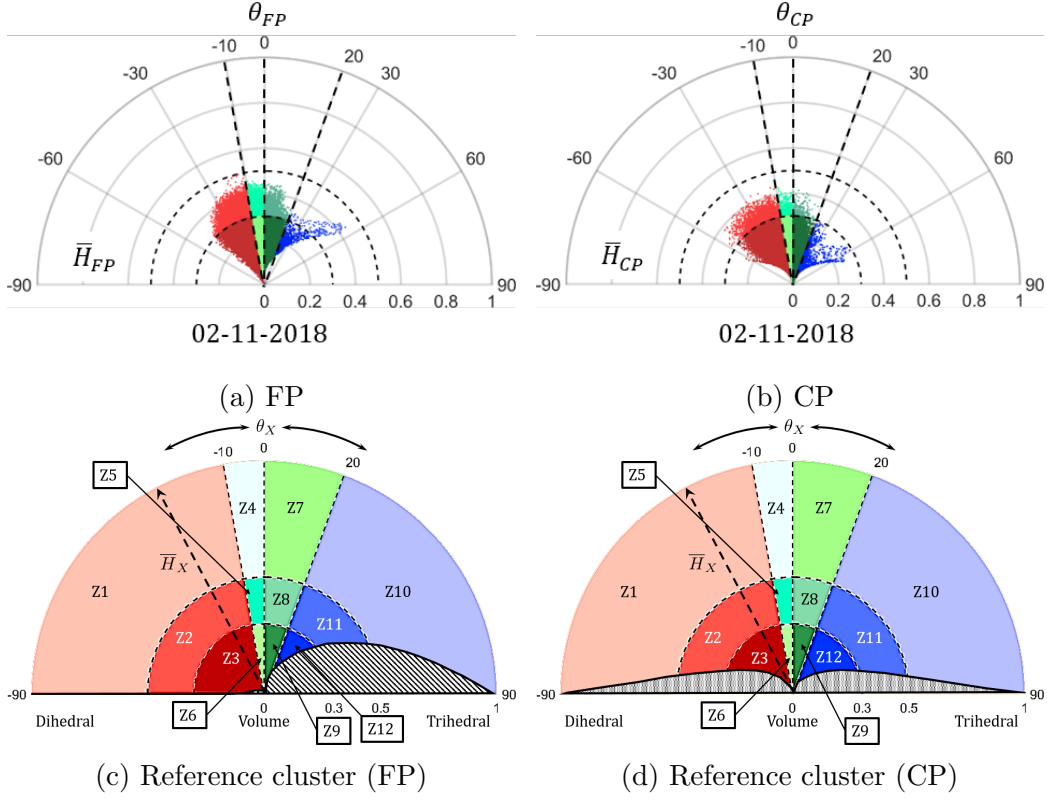


Figure 13: The \bar{H}_X/θ_X scatter plane for rice using FP and CP SAR data on 02-Nov.

464 rice canopy layer. The cluster in the Z12 zone corresponds to the scattering
 465 of the wave directly from the leaves of the uppermost canopy layer. During
 466 this time further decrease in even bounce scattering is evident.

467 On 26 Nov, the rice fields reached the maturity stage, and the grains
 468 become firm and heavy. At this point, the crop becomes dry, whereas the
 469 moisture content in grains remains $\approx 20\%$. Due to the weight of the grains,
 470 lodging of rice is usually visible in the fields due to which the morphological
 471 condition becomes further complicated than the dough stage. Hence, an
 472 additional increase in the scattering entropy during this period is apparent for

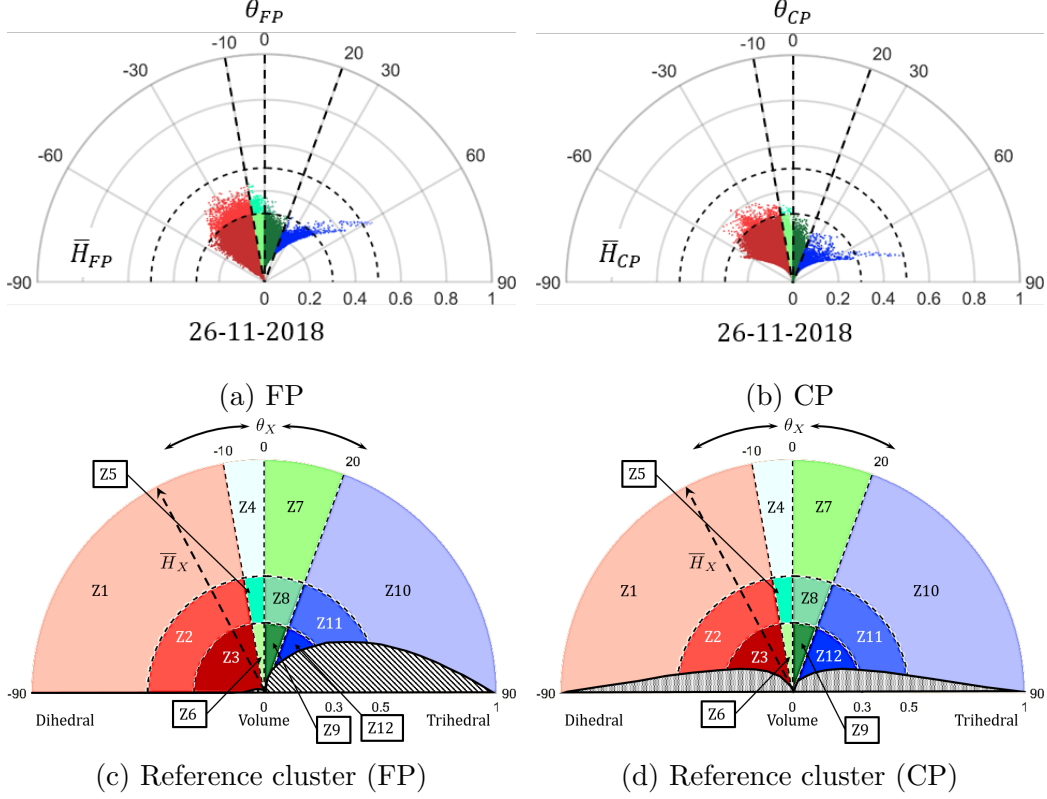


Figure 14: The \bar{H}_X/θ_X scatter plane for rice using FP and CP SAR data on 26-Nov.

both FP and CP SAR data. High densities of clusters in Z3, Z6, Z9, and Z12 zones can be noticed in figure 14a and figure 14b, which is due to scattering from the complex geometrical structure of rice at this stage. However, a small cluster can also be observed in the Z11 zone, which might be due to fully or partially harvested rice fields. At this stage, the highest contribution of multiple scattering mechanisms (73.23%) is profound due to the increase in scattering randomness within the SAR resolution cell. We performed hypothesis testing to show that these changes in the scattering mechanisms for different dates are related to rice phenological changes. In this regard, the

482 null hypothesis states that there exists no relationship between the changes in
483 the clusters and rice phenology (i.e., the change is due to randomness). The
484 p -values (95 % confidence level) as shown in Table 3 indicates that we can
485 reject the null hypothesis, and therefore, there is evidence that the changes
486 in the unsupervised clusters are due to rice phenology.

Table 3: Changes in the scattering mechanisms across different dates and between FP and CP data. we have considered (Z1, Z2, Z3) as even bounce scattering, (Z10, Z11, Z12) as odd bounce scattering and (Z4, Z5, Z6, Z7, Z8, Z9) as multiple bounce scattering. The dominant scattering mechanism(s) at each date is highlighted in bold font. Also, the p -values at 95 % significance level is provided

Dates	Modes	Even bounce scattering	Odd bounce scattering	Multiple bounce scattering	Growth Stage	p -value
05/07/2018	FP	0.90%	86.86%	12.24%	Bare field	2.30×10^{-11}
	CP	0.60%	88.28%	11.12%		2.18×10^{-11}
29/07/2018	FP	76.79%	4.48%	28.73%	Early tillering	2.20×10^{-16}
	CP	64.60%	2.10%	33.30%		2.18×10^{-15}
22/08/2018	FP	65.60%	2%	32.40%	Advanced tillering	2.20×10^{-16}
	CP	63.87%	2%	34.13%		1.96×10^{-16}
09/10/2018	FP	58.10%	1.88%	40.02%	Flowering	2.10×10^{-16}
	CP	56.33%	1.88%	41.79%		2.10×10^{-16}
02/11/2018	FP	39.40%	3%	57.60%	Early dough	2.40×10^{-14}
	CP	31.60%	2%	66.40%		1.82×10^{-14}
26/11/2018	FP	25.61%	1.16%	73.23%	Maturity	2.20×10^{-16}
	CP	16.76%	0.92%	82.30%		1.98×10^{-16}

487 It is noteworthy that the differences in the characterization capability be-
488 tween FP and CP SAR data depends on the type and geometry of the targets.
489 Moreover, the spatial heterogeneity induces the changes in the intensity of
490 the co-pol and cross-pol components. Hence, a change in the scattered EM
491 wave is sometimes evident between FP and CP SAR data.

492 6. Conclusions

493 In this study, we have proposed two scattering-type parameters, θ_{FP} and
494 θ_{CP} for identifying target scattering mechanism for both full (FP) and com-

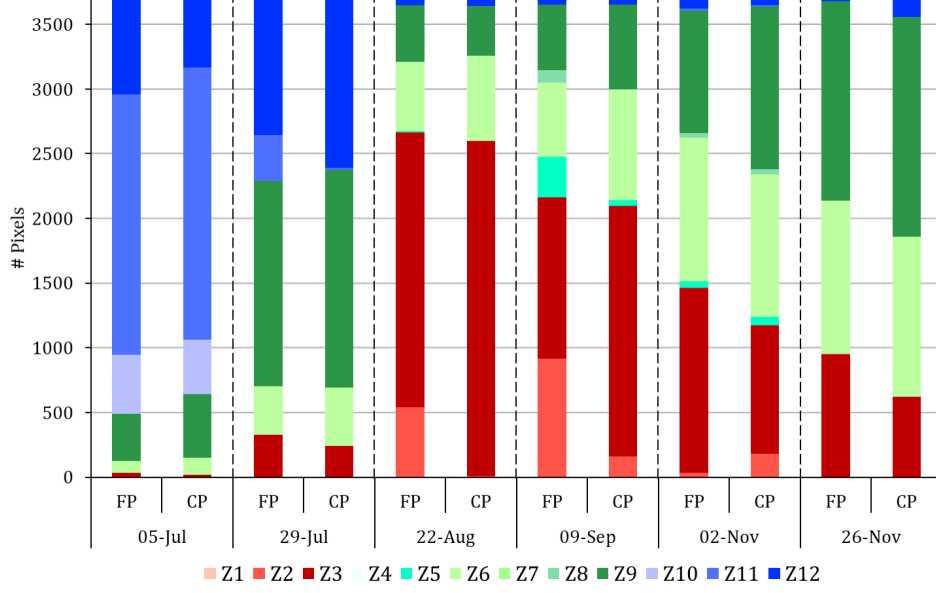


Figure 15: Variations in the number of pixels in different clusters for each date in FP and CP data.

495 pact polarimetric (CP) SAR data. These quantities are roll-invariant and
 496 vary in the range, -90° to 90° . In particular these two scattering-type pa-
 497 rameters jointly utilize the received antenna basis-invariant parameters, i.e.,
 498 the Barakat degree of polarization and the total scattering power (Span) and
 499 the elements of the coherency matrix. The two extreme values of their range
 500 correspond to even-bounce (-90°), and odd-bounce (90°) scattering mecha-
 501 nisms, while $\theta_{FP} = 0^\circ$ and $\theta_{CP} = 0^\circ$ denotes diffused scattering mechanism.
 502 Furthermore, θ_{FP} and θ_{CP} within the range, -10° to 0° indicates even-bounce
 503 multiple scattering components, and 0° to 20° denotes the odd-bounce mul-
 504 tiple scattering components.

505 In this study, we have suitably fulfilled our primary objective to char-
 506 acterize changes in the scattering mechanism with the advancement of crop
 507 phenological stages. We have used the scattering-type parameters for the

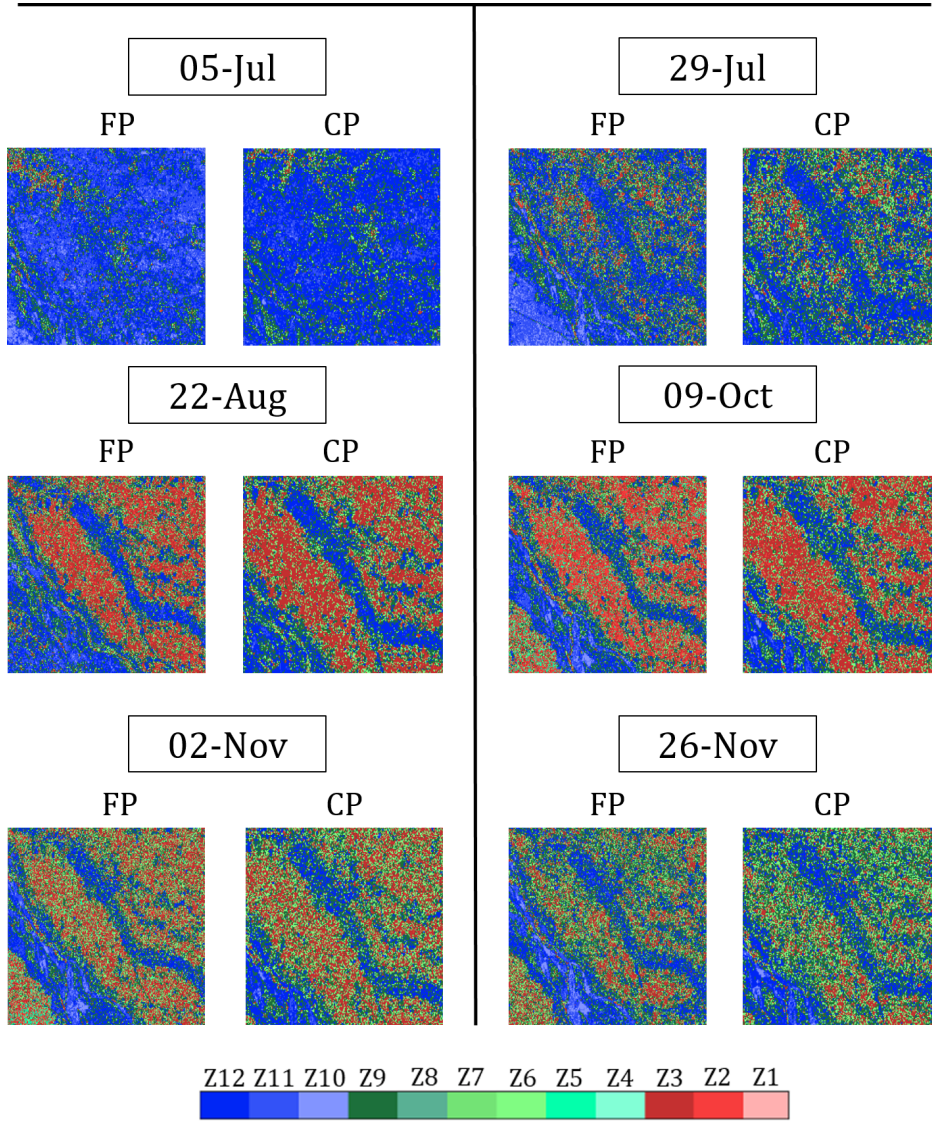


Figure 16: Variation of $\overline{H}_{FP}/\theta_{FP}$ and $\overline{H}_{CP}/\theta_{CP}$ clustered images for FP and CP over the study area. The growth stages are: 5-Jul: Bare field, 29-Jul: Early tillering, 22-Aug: Advanced tillering, 9-Oct: Flowering, 2-Nov: Early dough, and 26-Nov: Maturity

508 temporal analysis of rice over the Vijayawada test site in India using FP and
 509 CP SAR data. The sensitivities of θ_{FP} and θ_{CP} with growth stages of rice
 510 are significantly evident from this study. We have introduced novel new clus-

511 tering schemes, $\overline{H}_{\text{FP}}/\theta_{\text{FP}}$ and $\overline{H}_{\text{CP}}/\theta_{\text{CP}}$ in this study by utilizing θ_{FP} , θ_{CP} ,
512 and the scattering entropies, H_{FP} and H_{CP} . The clustering plane is split into
513 12 zones, where each zone represents a distinct dominant scattering mecha-
514 nism. In this regard, the $\overline{H}_{\text{FP}}/\theta_{\text{FP}}$ and $\overline{H}_{\text{CP}}/\theta_{\text{CP}}$ clustering planes provide
515 necessary information about targets without any *a priori* knowledge of the
516 scene.

517 The target characterization parameters as well as the clustering planes
518 provide information about changes in the scattering mechanism at different
519 crop phenological stage. They could be beneficial in providing essential in-
520 formation about crop conditions for engaging different cultivation measures.
521 Therefore, further investigation to track and map crop growth stages could
522 be conducted for different crop-types around the globe. The sensitivity of
523 these parameters for different crop geometry could be examined for differ-
524 ent incident angles using both FP and CP SAR data. We could adequately
525 utilize these parameters for the newly launched RADARSAT Constellation
526 Mission (RCM) and several upcoming missions.

527 **Appendix A. Roll-invariant parameters**

528 A parameter which is independent of target orientation angle along the
529 radar line of sight is called roll-invariant. In this section, we show the roll-
530 invariant nature of θ_{FP} and θ_{CP} .

531 *Appendix A.1. Roll-invariant nature of θ_{FP}*

532 To show that θ_{FP} is a roll-invariant parameter, let the coherency matrix
 533 \mathbf{T} be unitarily rotated by $\mathbf{R}(\Psi)$ as,

$$\mathbf{T}(\Psi) = \mathbf{R}(\Psi) \mathbf{T} \mathbf{R}(\Psi)^{-1}, \quad (\text{A.1})$$

534 where

$$\mathbf{R}(\Psi) = \begin{bmatrix} 1 & 0 & 0 \\ 0 & \cos 2\Psi & \sin 2\Psi \\ 0 & -\sin 2\Psi & \cos 2\Psi \end{bmatrix}. \quad (\text{A.2})$$

535 with,

$$\begin{aligned} T_{11}(\Psi) &= T_{11} \\ T_{22}(\Psi) &= T_{22} \cos^2(2\Psi) + T_{32} \cos(2\Psi) \sin(2\Psi) + \\ &\quad T_{23} \cos(2\Psi) \sin(2\Psi) + T_{33} \sin^2(2\Psi) \\ T_{33}(\Psi) &= T_{22} \sin^2(2\Psi) - T_{32} \cos(2\Psi) \sin(2\Psi) - \\ &\quad T_{23} \cos(2\Psi) \sin(2\Psi) + T_{33} \cos^2(2\Psi) \end{aligned} \quad (\text{A.3})$$

536 Therefore, $T_{11}(\Psi) - T_{22}(\Psi) - T_{33}(\Psi) = T_{11} - T_{22} - T_{33}$ and $T_{22}(\Psi) + T_{33}(\Psi) =$
 537 $T_{22} + T_{33}$ i.e., both $T_{11} - T_{22} - T_{33}$ and $T_{22} + T_{33}$ are independent of the
 538 unitary rotation by an angle Ψ . Alongside this, note that the total power
 539 i.e., $\text{Span} = T_{11}(\Psi) + T_{22}(\Psi) + T_{33}(\Psi) = T_{11} + T_{22} + T_{33} = \text{Tr}(\mathbf{T})$, and $|\mathbf{T}|$ are
 540 roll-invariant, where $|\cdot|$ is the determinant and $\text{Tr}(\cdot)$ is the trace of a matrix.
 541 Therefore, the 3D Barakat degree of polarization, $m_{\text{FP}} = \sqrt{1 - \frac{27|\mathbf{T}|}{(\text{Tr}(\mathbf{T}))^3}}$ is
 542 also independent of Ψ . Hence, we conclude that the proposed scattering-type

543 parameter for FP SAR,

$$\theta_{\text{FP}} = 2 \tan^{-1} \left(\frac{m_{\text{FP}} \text{Span} (T_{11} - T_{22} - T_{33})}{T_{11} (T_{22} + T_{33}) + m_{\text{FP}}^2 \text{Span}^2} \right) \quad (\text{A.4})$$

544 is independent of Ψ , i.e., it is a roll-invariant parameter.

545 *Appendix A.2. Roll-invariant nature of θ_{CP}*

546 The 2×2 covariance matrix can be expressed in terms of the elements of
 547 the Stokes vector $\vec{\mathbf{S}} = [S_0, S_1, S_2, S_3]$ as

$$\mathbf{C}_2 = \frac{1}{2} \begin{bmatrix} S_0 + S_1 & S_2 + iS_3 \\ S_2 - iS_3 & S_0 - S_1 \end{bmatrix}. \quad (\text{A.5})$$

548 Let the \mathbf{C}_2 matrix be unitarily rotated by $\mathbf{R}(\Psi)$ as $\mathbf{C}_2(\Psi) = \mathbf{R}(\Psi) \mathbf{C}_2 \mathbf{R}(\Psi)^{-1}$,
 549 where the rotation matrix is,

$$\mathbf{R}(\Psi) = \begin{bmatrix} \cos(\Psi) & -\sin(\Psi) \\ \sin(\Psi) & \cos(\Psi) \end{bmatrix}. \quad (\text{A.6})$$

550 The elements of the $\mathbf{C}_2(\Psi)$ matrix are:

$$\begin{aligned}
c_{11}(\Psi) &= \cos^2 \Psi (S_0 + S_1) - \cos \Psi \sin \Psi (S_2 - iS_3) - \\
&\quad \cos \Psi \sin \Psi (S_2 + iS_3) + \sin^2 \Psi (S_0 - S_1) \\
c_{12}(\Psi) &= \cos \Psi \sin \Psi (S_0 + S_1) - \sin^2 \Psi (S_2 - iS_3) + \\
&\quad \cos^2 \Psi (S_2 + iS_3) - \cos \Psi \sin \Psi (S_0 - S_1) \\
c_{21}(\Psi) &= \cos \Psi \sin \Psi (S_0 + S_1) + \cos^2 \Psi (S_2 - iS_3) - \\
&\quad \sin^2 \Psi (S_2 + iS_3) - \cos \Psi \sin \Psi (S_0 - S_1) \\
c_{22}(\Psi) &= \sin^2 \Psi (S_0 + S_1) - \cos \Psi \sin \Psi (S_2 - iS_3) - \\
&\quad \cos \Psi \sin \Psi (S_2 + iS_3) + \cos^2 \Psi (S_0 - S_1).
\end{aligned} \tag{A.7}$$

551 The total power $S_0 = c_{11}(\Psi) + c_{22}(\Psi)$ and the fourth element of the Stokes
552 vector $S_3 = -i(c_{12}(\Psi) - c_{21}(\Psi))$ are independent of the rotation angle Ψ .
553 Since S_0 and S_3 are independent of Ψ , then $\text{SC} = (S_0 - S_3)/2$ and $\text{OC} =$
554 $(S_0 + S_3)/2$ are also independent of Ψ , i.e. both parameters are roll-invariant.
555 Alongside this, note that $|\mathbf{C}_2|$ and $\text{Tr}(\mathbf{C}_2)$ are roll-invariant, where $|\cdot|$ is the
556 determinant and $\text{Tr}(\cdot)$ is the trace of a matrix. Therefore, the 2D Barakat
557 degree of polarization, $m_{\text{CP}} = \sqrt{1 - \frac{4|\mathbf{C}_2|}{(\text{Tr}(\mathbf{C}_2))^2}}$ is also roll-invariant. Hence,
558 we conclude that the proposed scattering-type parameter for CP SAR,

$$\theta_{\text{CP}} = 2 \tan^{-1} \left(\frac{m_{\text{CP}} S_0 (\text{OC} - \text{SC})}{\text{OC} \times \text{SC} + m_{\text{CP}}^2 S_0^2} \right) \tag{A.8}$$

559 is independent of Ψ , i.e., it is a roll-invariant parameter.

560 Appendix B. Simulating CP data from FP data

561 The scattering matrix \mathbf{S} for the FP SAR data can be written as,

$$\mathbf{S} = \begin{bmatrix} S_{HH} & S_{HV} \\ S_{VH} & S_{VV} \end{bmatrix} \quad (\text{B.1})$$

562 For general transmit and linear receive, the scattering vector $\vec{k}_{\theta,\chi}$ can be
563 written in terms of the elements of the \mathbf{S} matrix as,

$$\vec{k}_{\theta,\chi} = \begin{bmatrix} \cos(\chi) (\cos(\theta) S_{HH} + \sin(\theta) S_{HV}) + i \sin(\chi) (\sin(\theta) S_{HH} - \cos(\theta) S_{HV}) \\ \cos(\chi) (\cos(\theta) S_{VH} + \sin(\theta) S_{VV}) + i \sin(\chi) (\sin(\theta) S_{VH} - \cos(\theta) S_{VV}) \end{bmatrix} \quad (\text{B.2})$$

564 where, χ and θ are ellipticity and orientation angles respectively (Sabry and
565 Vachon, 2013). For a general transmit and general receive mode (GTGR),
566 the scattering vector can be related as,

$$\vec{k}_{\theta_r, \chi_r | \theta, \chi} = \mathbf{U}_{\theta_r, \chi_r} \vec{k}_{\theta, \chi} \quad (\text{B.3})$$

567 where,

$$\mathbf{U}_{\theta_r, \chi_r} = \begin{bmatrix} \cos(\theta_r) \cos(\chi_r) + i \sin(\theta_r) \sin(\chi_r) & \sin(\theta_r) \cos(\chi_r) - i \cos(\theta_r) \sin(\chi_r) \\ -\sin(\theta_r) \cos(\chi_r) - i \cos(\theta_r) \sin(\chi_r) & \cos(\theta_r) \cos(\chi_r) - i \sin(\theta_r) \sin(\chi_r) \end{bmatrix} \quad (\text{B.4})$$

568 The 2×2 covariance matrix for GTGR becomes,

$$\mathbf{C}p(\theta_r, \chi_r | \theta, \chi) = \mathbf{U}_{\theta_r, \chi_r} \mathbf{C}p(\theta, \chi) \mathbf{U}_{\theta_r, \chi_r}^\dagger \quad (\text{B.5})$$

569 where,

$$\mathbf{C}p(\theta, \chi) = \langle \vec{k}_{\theta, \chi} \vec{k}_{\theta, \chi}^\dagger \rangle \quad (\text{B.6})$$

570 The coherent correlation between polarimetric channels or the inter-polarimetric
571 correlation factors can be represented as,

$$\gamma_H = \frac{\langle S_{HH} S_{HV}^* \rangle}{\sqrt{\langle |S_{HH}|^2 \rangle} \sqrt{\langle |S_{HV}|^2 \rangle}}; \quad \gamma_V = \frac{\langle S_{VV} S_{HV}^* \rangle}{\sqrt{\langle |S_{VV}|^2 \rangle} \sqrt{\langle |S_{HV}|^2 \rangle}}; \quad \gamma_{HV} = \frac{\langle S_{HH} S_{VV}^* \rangle}{\sqrt{\langle |S_{HH}|^2 \rangle} \sqrt{\langle |S_{VV}|^2 \rangle}} \quad (\text{B.7})$$

572 along with the ratio factors,

$$a = \sqrt{\frac{\langle |S_{HV}|^2 \rangle}{\langle |S_{HH}|^2 \rangle}} = \sqrt{\frac{\langle \sigma_{HV}^0 \rangle}{\langle \sigma_{HH}^0 \rangle}}; \quad b = \sqrt{\frac{\langle |S_{HV}|^2 \rangle}{\langle |S_{VV}|^2 \rangle}} = \sqrt{\frac{\langle \sigma_{HV}^0 \rangle}{\langle \sigma_{VV}^0 \rangle}}; \quad c = \frac{a}{b} = \sqrt{\frac{\langle |S_{VV}|^2 \rangle}{\langle |S_{HH}|^2 \rangle}} = \sqrt{\frac{\langle \sigma_{VV}^0 \rangle}{\langle \sigma_{HH}^0 \rangle}} \quad (\text{B.8})$$

where σ^0 represents the normalized radar cross section. Using (B.6), (B.7) and (B.8), the elements of the 2×2 covariance matrix $\mathbf{C}p(\theta, \chi)$ for the General Transmit and Linear Received (GTLR) can be expressed by,

$$Cp_{11}(\theta, \chi) = \frac{1}{2} \langle |S_{HH}|^2 \rangle \{ (1 + \cos(2\theta) \cos(2\chi)) + (1 - \cos(2\theta) \cos(2\chi)) a^2 + \sin(2\theta) \cos(2\chi) a (\gamma_H + \gamma_H^*) + i \sin(2\chi) a (\gamma_H - \gamma_H^*) \} \quad (\text{B.9})$$

$$Cp_{12}(\theta, \chi) = Cp_{21}^*(\theta, \chi) = \frac{1}{2} \langle |S_{HH}|^2 \rangle \{ (1 + \cos(2\theta) \cos(2\chi)) a \gamma_H + (1 - \cos(2\theta) \cos(2\chi)) a c \gamma_V^* + \sin(2\theta) \cos(2\chi) (c \gamma_{HV} + a^2) + i \sin(2\chi) (c \gamma_{HV} - a^2) \} \quad (\text{B.10})$$

$$Cp_{22}(\theta, \chi) = \frac{1}{2} \langle |S_{HH}|^2 \rangle \{ (1 + \cos(2\theta) \cos(2\chi)) a^2 + (1 - \cos(2\theta) \cos(2\chi)) c^2 + \sin(2\theta) \cos(2\chi) ac (\gamma_V + \gamma_V^*) - i \sin(2\chi) ac (\gamma_V - \gamma_V^*) \} \quad (\text{B.11})$$

Therefore, for right circular polarized transmit wave, we have considered, $\chi = -45^\circ$ and $\theta = 0^\circ$. In this work, we have used the European Space Agency's (ESA) open-source toolbox for polarimetric SAR data processing and education PolSARpro (Polarimetric SAR Data Processing and Education Toolbox). We have used this toolbox for simulating CP data from FP SAR data.

Appendix C. Software/Codes to extract FP and CP parameters

We obtain the 3×3 coherency matrix, \mathbf{T} from the full-polarimetric SAR data using the PolSARpro software. The compact polarimetric data is simulated using the same software by assuming right-hand circular polarized transmit wave (i.e., $\chi = -45^\circ$), where χ is the ellipticity parameter of the polarization ellipse.

All the parameters used in this study (i.e., m_{FP} , m_{CP} , θ_{FP} , θ_{CP} , H_{FP} , and H_{CP}) are computed using scripts developed in MATLAB R2019b environment as shown in figure C.17. For the full-polarimetry data, we read the 9 elements (i.e., 3 positive real diagonal elements and 3 complex off-diagonal elements) of the \mathbf{T} matrix while for compact-polarimetry data, we read the 4 elements (i.e., 2 positive real diagonal elements and 1 complex off-diagonal element) of the \mathbf{C}_2 matrix. Thereafter, using array solution and iteration methods, we compute the spatial distribution of these parameters. The codes are available at: <http://github.com/Subho07/Temporal-clustering-of-SAR-data/>

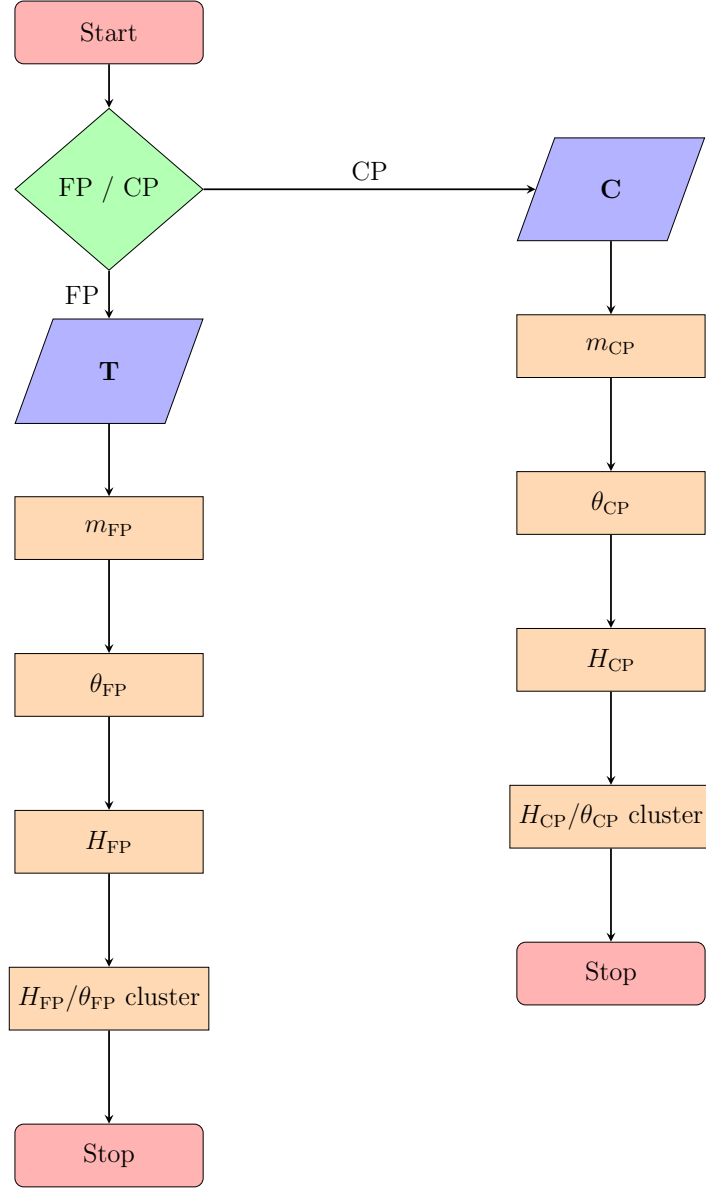


Figure C.17: Flow chart for computing the Barakat degree of polarization (m_{FP} , m_{CP}), target characterizing parameters (θ_{FP} , θ_{CP}) and scattering entropy (H_{FP} , H_{CP}) for FP and CP data using MATLAB R2019b environment.

594 **Acknowledgements**

595 The authors want to thank Prof. Alejandro C. Frery, School of Mathe-
596 matics and Statistics, Victoria University of Wellington, New Zealand, for
597 helping us with the statistical analysis of the clustering scheme. The authors
598 would like to thank the Canadian Space Agency and MAXAR Technolo-
599 gies Ltd. (formerly MDA) for providing RADARSAT-2 images through the
600 Joint Experiment for Crop Assessment and Monitoring (JECAM) Network.
601 The authors are also thankful to Andhra Pradesh Space Application Centre
602 (APSAC), ITE & C Department, Government of Andhra Pradesh for their
603 support during field campaigns. This work was supported in part by the
604 Spanish Ministry of Science, Innovation and Universities, the State Agency of
605 Research (AEI), and the European Funds for Regional Development (EFRD)
606 under Project TEC 2017-85244-C 2-1-P. The work of Dipankar Mandal was
607 supported by the Ministry of Human Resource Development, Government of
608 India (New Delhi, India) towards his Ph.D. assistantship through grant no.
609 RSPHD0210.

610 **References**

- 611 Ainsworth, T., Kelly, J., Lee, J.-S., 2009. Classification comparisons between
612 dual-pol, compact polarimetric and quad-pol SAR imagery. *ISPRS Journal*
613 *of Photogrammetry and Remote Sensing* 64 (5), 464–471.
- 614 Antropov, O., Rauste, Y., Hame, T., 2011. Volume scattering modeling in
615 PolSAR decompositions: Study of ALOS PALSAR data over boreal forest.
616 *IEEE Transactions on Geoscience and Remote Sensing* 49 (10), 3838–3848.

- 617 Ballester-Berman, J. D., Lopez-Sanchez, J. M., 2011. Time series of hybrid-
618 polarity parameters over agricultural crops. *IEEE Geoscience and Remote*
619 *Sensing Letters* 9 (1), 139–143.
- 620 Barakat, R., 1977. Degree of polarization and the principal idempotents of
621 the coherency matrix. *Optics Communications* 23 (2), 147–150.
- 622 Barakat, R., 1983. n-fold polarization measures and associated thermody-
623 namic entropy of N partially coherent pencils of radiation. *Optica Acta:*
624 *International Journal of Optics* 30 (8), 1171–1182.
- 625 Brisco, B., Li, K., Tedford, B., Charbonneau, F., Yun, S., Murnaghan, K.,
626 2013. Compact polarimetry assessment for rice and wetland mapping. *In-*
627 *ternational journal of remote sensing* 34 (6), 1949–1964.
- 628 Charbonneau, F., Brisco, B., Raney, R., McNairn, H., Liu, C., Vachon, P.,
629 Shang, J., DeAbreu, R., Champagne, C., Merzouki, A., et al., 2010. Com-
630 pact polarimetry overview and applications assessment. *Canadian Journal*
631 *of Remote Sensing* 36 (sup2), S298–S315.
- 632 Cloude, S. R., Goodenough, D. G., Chen, H., 2011. Compact decomposition
633 theory. *IEEE Geoscience and Remote Sensing Letters* 9 (1), 28–32.
- 634 Cloude, S. R., Pottier, E., 1997. An entropy based classification scheme for
635 land applications of polarimetric SAR. *IEEE transactions on geoscience*
636 *and remote sensing* 35 (1), 68–78.
- 637 Davidson, M. W., Le Toan, T., Mattia, F., Satalino, G., Manninen, T.,
638 Borgeaud, M., 2000. On the characterization of agricultural soil roughness

639 for radar remote sensing studies. *IEEE Transactions on Geoscience and*
640 *Remote Sensing* 38 (2), 630–640.

641 De Bernardis, C. G., Vicente-Guijalba, F., Martinez-Marin, T., Lopez-
642 Sanchez, J. M., 2015. Estimation of key dates and stages in rice crops
643 using dual-polarization SAR time series and a particle filtering approach.
644 *IEEE Journal of Selected Topics in Applied Earth Observations and Re-*
645 *mote Sensing* 8 (3), 1008–1018.

646 Dey, S., Bhattacharya, A., Ratha, D., Mandal, D., Frery, A. C., 2020. Target
647 characterization and scattering power decomposition for full and compact
648 polarimetric SAR data. *IEEE Transactions on Geoscience and Remote*
649 *Sensing*.

650 Guo, X., Li, K., Shao, Y., Wang, Z., Li, H., Yang, Z., Liu, L., Wang, S.,
651 2018. Inversion of rice biophysical parameters using simulated compact
652 polarimetric SAR C-band data. *Sensors* 18 (7), 2271.

653 He, Z., Li, S., Wang, Y., Dai, L., Lin, S., 2018. Monitoring rice phenology
654 based on backscattering characteristics of multi-temporal RADARSAT-2
655 datasets. *Remote Sensing* 10 (2), 340.

656 Kumar, V., Mandal, D., Bhattacharya, A., Rao, Y., 2020. Crop charac-
657 terization using an improved scattering power decomposition technique
658 for compact polarimetric sar data. *International Journal of Applied Earth*
659 *Observation and Geoinformation* 88, 102052.

660 Lee, J.-S., Pottier, E., 2009. *Polarimetric radar imaging: from basics to*
661 *applications*. CRC press.

- 662 Lopez-Sanchez, J. M., Ballester-Berman, J. D., Hajnsek, I., 2011. First
663 results of rice monitoring practices in Spain by means of time series of
664 TerraSAR-X dual-pol images. *IEEE Journal of selected topics in applied*
665 *earth observations and remote sensing* 4 (2), 412–422.
- 666 Lopez-Sanchez, J. M., Cloude, S. R., Ballester-Berman, J. D., 2012. Rice
667 phenology monitoring by means of SAR polarimetry at X-band. *IEEE*
668 *Transactions on Geoscience and Remote Sensing* 50 (7), 2695–2709.
- 669 Lopez-Sanchez, J. M., Vicente-Guijalba, F., Ballester-Berman, J. D., Cloude,
670 S. R., 2014. Polarimetric response of rice fields at C-band: Analysis and
671 phenology retrieval. *IEEE Transactions on Geoscience and Remote Sensing*
672 52 (5), 2977–2993.
- 673 Mandal, D., Kumar, V., Rao, Y., Bhattacharya, A., Ramana, K.,
674 2019. Experimental field campaigns at Vijayawada test site. Tech. Rep.
675 MRS2019TR02, Microwave Remote Sensing Lab, India.
676 URL <http://doi.org/10.17605/OSF.IO/DN3E8>
- 677 Mandal, D., Kumar, V., Ratha, D., Lopez-Sanchez, J. M., Bhattacharya, A.,
678 McNairn, H., Rao, Y., Ramana, K., 2020. Assessment of rice growth condi-
679 tions in a semi-arid region of India using the generalized radar vegetation
680 index derived from Radarsat-2 polarimetric SAR data. *Remote Sensing of*
681 *Environment* 237, 111561.
- 682 McNairn, H., Jiao, X., Pacheco, A., Sinha, A., Tan, W., Li, Y., 2018. Esti-
683 mating canola phenology using synthetic aperture radar. *Remote sensing*
684 *of environment* 219, 196–205.

- 685 McNairn, H., Shang, J., 2016. A review of multitemporal synthetic aper-
686 ture radar (SAR) for crop monitoring. In: Multitemporal Remote Sensing.
687 Springer, pp. 317–340.
- 688 Paloscia, S., 2002. A summary of experimental results to assess the contribu-
689 tion of SAR for mapping vegetation biomass and soil moisture. *Canadian*
690 *Journal of Remote Sensing* 28 (2), 246–261.
- 691 Praks, J., Koeniguer, E. C., Hallikainen, M. T., 2009. Alternatives to tar-
692 get entropy and alpha angle in SAR polarimetry. *IEEE Transactions on*
693 *Geoscience and Remote Sensing* 47 (7), 2262–2274.
- 694 Raney, R. K., 2007. Hybrid-polarity SAR architecture. *IEEE Transactions*
695 *on Geoscience and Remote Sensing* 45 (11), 3397–3404.
- 696 Raney, R. K., Cahill, J. T., Patterson, G. W., Bussey, D. B. J., 2012. The m-
697 chi decomposition of hybrid dual-polarimetric radar data with application
698 to lunar craters. *Journal of Geophysical Research: Planets* 117 (E12).
- 699 Ratha, D., Pottier, E., Bhattacharya, A., Frery, A. C., 2019. A PolSAR scat-
700 tering power factorization framework and novel roll-invariant parameter-
701 based unsupervised classification scheme using a geodesic distance. *IEEE*
702 *Transactions on Geoscience and Remote Sensing*, 1–17.
- 703 Sabry, R., Vachon, P. W., 2013. A unified framework for general compact and
704 quad polarimetric SAR data and imagery analysis. *IEEE Transactions on*
705 *Geoscience and Remote Sensing* 52 (1), 582–602.
- 706 Touzi, R., Hurley, J., Vachon, P. W., 2015. Optimization of the degree of

707 polarization for enhanced ship detection using polarimetric RADARSAT-2.
708 IEEE Transactions on Geoscience and Remote Sensing 53 (10), 5403–5424.

709 Touzi, R., Omari, K., Sleep, B., Jiao, X., 2018. Scattered and received
710 wave polarization optimization for enhanced peatland classification and
711 fire damage assessment using polarimetric PALSAR. IEEE Journal of Se-
712 lected Topics in Applied Earth Observations and Remote Sensing 11 (11),
713 4452–4477.

714 Uppala, D., Kothapalli, R. V., Poloju, S., Mullapudi, S. S. V. R., Dad-
715 hwal, V. K., 2015. Rice crop discrimination using single date RISAT1 hy-
716 brid (RH, RV) polarimetric data. Photogrammetric Engineering & Remote
717 Sensing 81 (7), 557–563.

718 Wiseman, G., McNairn, H., Homayouni, S., Shang, J., 2014. RADARSAT-
719 2 polarimetric SAR response to crop biomass for agricultural production
720 monitoring. IEEE Journal of Selected Topics in Applied Earth Observa-
721 tions and Remote Sensing 7 (11), 4461–4471.

722 Xie, L., Zhang, H., Wu, F., Wang, C., Zhang, B., 2015. Capability of rice
723 mapping using hybrid polarimetric SAR data. IEEE Journal of Selected
724 Topics in Applied Earth Observations and Remote Sensing 8 (8), 3812–
725 3822.

726 Yang, Z., Li, K., Liu, L., Shao, Y., Brisco, B., Li, W., 2014. Rice growth mon-
727 itoring using simulated compact polarimetric C band SAR. Radio Science
728 49 (12), 1300–1315.

- 729 Yin, J., Moon, W. M., Yang, J., 2015. Novel model-based method for identi-
730 fication of scattering mechanisms in polarimetric SAR data. IEEE Trans-
731 actions on Geoscience and Remote Sensing 54 (1), 520–532.
- 732 Yin, J., Papathanassiou, K. P., Yang, J., 2019. Formalism of compact po-
733 larimetric descriptors and extension of the $\Delta\alpha B/\alpha B$ method for general
734 compact-pol SAR. IEEE Transactions on Geoscience and Remote Sensing,
735 1–14.
- 736 Yonezawa, C., Negishi, M., Azuma, K., Watanabe, M., Ishitsuka, N., Ogawa,
737 S., Saito, G., 2012. Growth monitoring and classification of rice fields using
738 multitemporal RADARSAT-2 full-polarimetric data. International journal
739 of remote sensing 33 (18), 5696–5711.
- 740 Yuzugullu, O., Erten, E., Hajnsek, I., 2015. Rice growth monitoring by means
741 of X-band co-polar SAR: Feature clustering and bbch scale. IEEE Geo-
742 science and Remote Sensing Letters 12 (6), 1218–1222.